



Ecole Nationale Supérieure de Physique, Électronique, Matériaux (Phelma) –
Grenoble INP

European Master in Nuclear Energy (EMINE)
2020-2021

MASTER THESIS

**Investigation of a Neural Network Algorithm for In-Situ X-ray
Tomography**

Justice NWADE

SUPERVISORS:

M. Luc SALVO – luc.salvo@grenoble-inp.fr

M. Pierre LHUISSIER – pierre.lhuissier@simap.grenoble-inp.fr

ACADEMIC MENTOR:

M. Ronald PHLIPO

RESEARCH LABORATORY:

SIMaP – Science et Ingénierie des Matériaux et Procédés

August, 2021

Contents

Abstract	2
Acknowledgement	3
CHAPTER I: CONTEXT	4
CHAPTER II: STATE OF THE ART	7
Principles of X-ray Tomography	7
Image Reconstruction:	8
Convolutional Neural Network algorithm	8
Mixed-Scale Dense Convolutional Neural Network (M-SDNet) Algorithm	10
Image Comparison	12
CHAPTER III: MATERIALS AND METHODS	14
Al-Cu-Si Scanned at ESRF:	14
316L(N) Steel	15
Al-Cu-Si Laboratory Tomography	16
Image Processing	18
Image Reconstruction:	18
Zone Selection:	18
Image Filtering	20
Segmentation	20
Parameter Analysis:	20
M-SDNet Application	21
CHAPTER IV: RESULTS AND DISCUSSION	23
Qualitative Inspection of grey level images	23
Qualitative Inspection of Binary Images:	25
Quantitative Comparison of IA Reconstructed Volumes:	27
General Metrics:	27
Number and Volume Fraction of Pores:	28
3D Pore Comparison:	29
Influence of Number of Projections with Training on Binary Images (Al-Cu-Si sample)	35
Analysis of Network Output Volumes:	37
Training on 316L(N) Data	40
Effect of Resolution: Improving Lab Experimental Data	41
Improving In-Situ Experimental Data	42
CHAPTER V: CONCLUSION AND PERSPECTIVES	43
Appendix:	45
References	49

Abstract

X-ray tomography is an important non-destructive technique for materials structure analysis. In certain applications, especially during in-situ experiments, the constraints posed by the experimental conditions limit the image quality obtainable from the limited data acquired. Commonly used direct image reconstruction algorithms tend to produce images with insufficient accuracy when fed with limited data, while the more accurate iterative algorithms introduce the challenge of high computational cost. A proposed alternative is the use of machine learning to improve the image quality of direct algorithms. The Mixed-Scale Dense convolutional neural network algorithm (M-SDNet) was therefore utilized in this study to quantitatively investigate its effect in improving the image quality of image reconstructions using direct algorithms, for in-situ tomography. Results are shown for the effect of number of projections, threshold values, and resolution, for data acquired in laboratory conditions. The cavities present in the studied sample were the focus of the quantitative analysis, where parameters like number of cavities, sphericity, and volume fraction were tracked across the output images from using the M-SDNet algorithm. Two different training strategies of M-SDNet; segmentation training and regression training, were compared with the segmentation training proving to better at reproducing cavities in the output images. The reduction on the number of projections and the required scan time suggest that the Mixed-Scale Dense networks are able to significantly improve the accuracy of image reconstructions, and thus suitable to overcome the experimental constraints during in-situ tomography.

Acknowledgement

I would like to thank my supervisors Luc Salvo and Pierre Lhuissier for the opportunity to intern in SIMaP, Grenoble, for the awesome supervision throughout the course of my internship, and for the lessons received during the EMINE program. Without their guidance this thesis would not have been possible.

I want also to express my gratitude to Dr. Daniel Pelt of the CWU, Netherlands, who generously allowed access to the M-SDNet algorithm and explained the concept behind its use. To my colleagues Sahil Valiyev and Oguz Ozdemir, who provided me important data and helped fine-tune my codes, and were exceptionally helpful throughout my internship.

My deepest appreciation goes to my family. Their support during this year and especially during confinement has been priceless. Their love and care albeit long-distance, kept me sane throughout the chaos occasioned by the pandemic.

The EMINE program has been a life transforming experience, and the people I met on it will stick with me forever. I will always be grateful for everything I have learned on this experience.

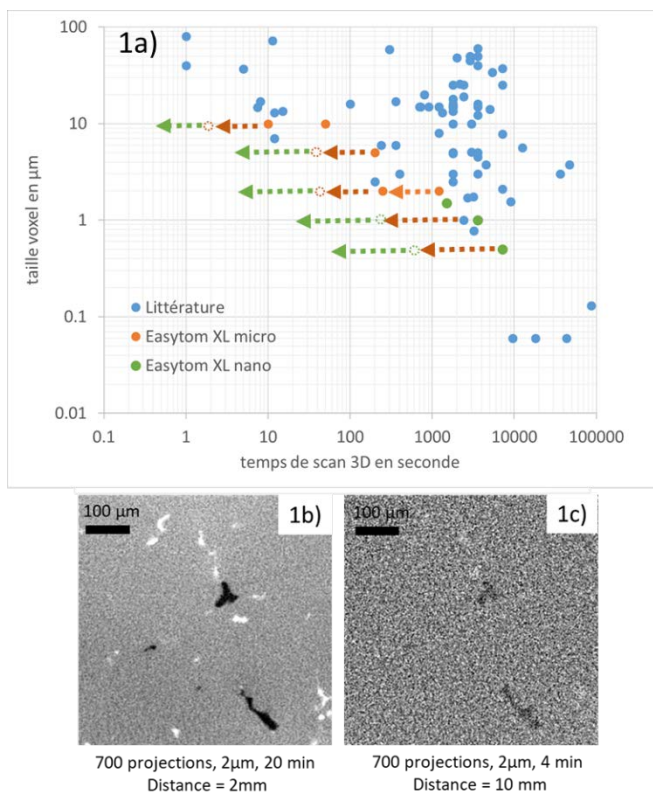
CHAPTER I: CONTEXT

X-ray tomography is a non-destructive 3D imaging technique that uses x-rays to probe into material internal structure.

During x-ray tomography, the sample is placed on a stand and rotated relative to the x-ray source. The x-ray photons pass through the sample, interacting with the material and leaving with less intensity than the initial. This process is called attenuation and explained by the Lambert-Beer's law. A detector detects the attenuated photons, producing an image of the object cast on it at the specified angle – called a projection. Reconstruction algorithms are afterward used to produce the 3D image of the internal surface of the scanned object.

Tomography is usually carried out with a laboratory x-ray source or in a synchrotron radiation facility. In-situ X-ray tomography (in the laboratory or synchrotron) in materials science has developed because it allows in-situ monitoring of microstructural changes during thermal processing (drying, solidification), during thermomechanical processing (cold or hot damage) with advanced quantitative analysis [1] [2] [3]. The technique is compatible with the multi-resolution analyses required in the field of hot forming and additive manufacturing.

There have been many developments in in-situ X-ray tomography for synchrotron sources, including at the nanoscale, opening up previously unimagined perspectives.



Laboratory sources have not been left behind and the Figure 1a) shows a non-exhaustive but representative overview of the various in situ studies (scan time as a function of voxel size in µm). Times of the order of a few tens of seconds for a scan are achievable for medium resolutions ($> 10\mu\text{m}$) but are too long for in situ tests at resolutions of the order of $2\mu\text{m}$. While a 20-minute acquisition at $2\mu\text{m}$ on the EASYTOMXL tomograph (in SiMaP laboratory) is possible and gives a correct image (Figure 1b) when the sample is close to the source. However, it becomes very noisy if the sample is offset by 10 mm (Figure 1c), the distance needed to put sample environments such as a furnace or a traction machine).

Figure 1: Developments in in-situ tomography studies

Reconstruction algorithms based on neural networks, developed by LIACS [4], allow a considerable reduction in the number of projections (gain by a factor of 5 to 10, see arrows in

Figure 1a). Furthermore, this algorithm can be used to increase resolution from medium resolution scans and to reduce noise on the images acquired and therefore in exposure time. These promising algorithms have often been validated on static scans and compared to conventional reconstruction techniques, usually by a simple qualitative analysis of the grey-scale images [5]. Their development requires a rigorous and complete study of their advantages and disadvantages on laboratory X-ray sources, synchrotron X-ray sources and neutron sources during static and in situ acquisitions that require quantitative 3D analyses. During the course of this internship, we investigate the potential power of CNN on data obtained from 316L(N) sample for nuclear application and Aluminium alloys for automotive application. We will thus compare high resolution scans to “degraded scans” reconstructed with CNN algorithm using adequate metrics on segmented volumes.

In-situ laboratory tomography suffer from the unique challenge posed by the space limitation for the furnace or compacting device, and the need to acquire high resolution images in the shortest scan time when sample is thus placed far from the source. Due to the divergence of the beam the number of photons in the detector is far less than in classical configuration leading to noisy images. To obtain high image resolution, parameters such as Source-Detector Distance (SDD), Source-to-Object Distance (SOD), and the camera pixel size of the detector have to be optimized.

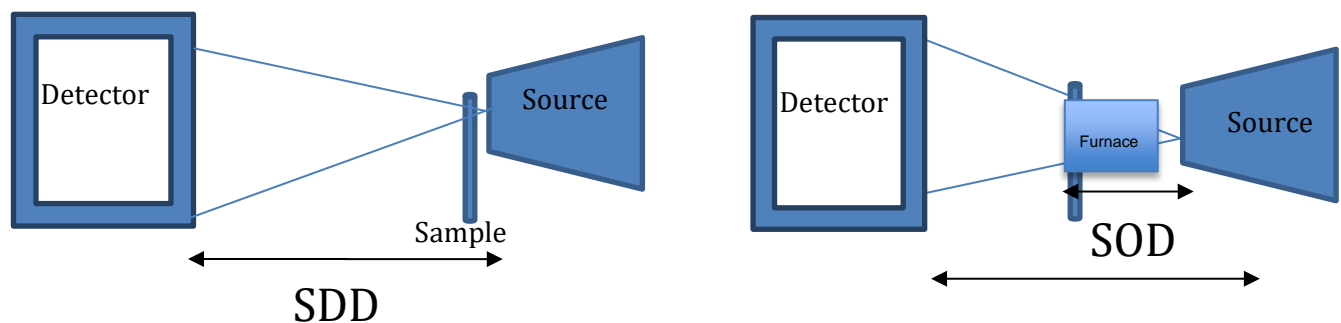


Figure 2. Equipment set-up for normal (left) and in-situ (right) tomography.

Another unique challenge involved in imaging both at synchrotron sources and in the laboratory is the need for storage space for acquired images. CNNs have been proposed to reconstruct images from limited data thereby freeing up storage space.

The objectives of the study are to quantitatively investigate the potentiality of the Mixed Scale Dense convolutional neural network algorithm (M-SDNet) for in-situ tomography. The application of the algorithm is expected to;

- (i) Reduce the number of projections needed for image reconstruction
- (ii) Increase the resolution of images acquired from in-situ tomography
- (iii) Reduce the acquisition time.

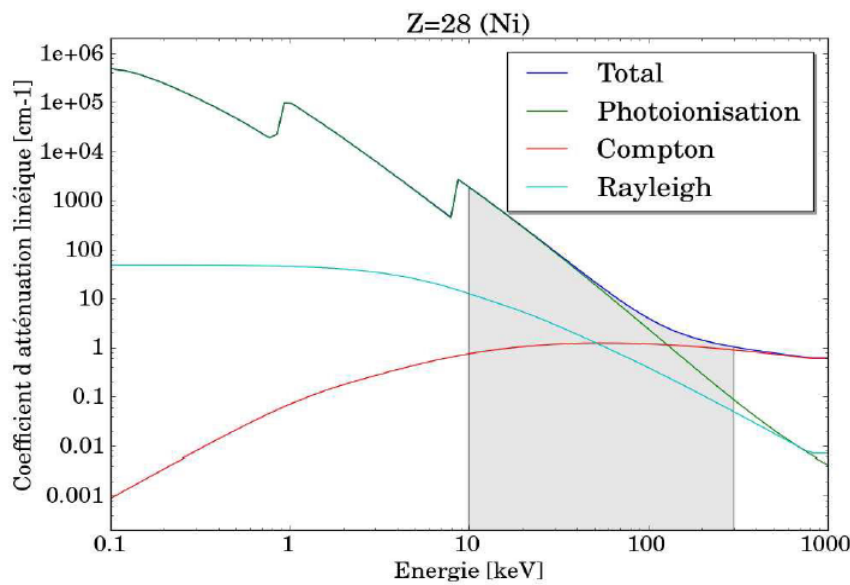
As a consequence, the following would be achieved from the use of the algorithm for in-situ tomography.

- (i) Reduction in the amount of data, thereby eliminating the need for more storage space for acquired images.
- (ii) Reduction in the dose scanned samples are exposed to. This is crucial for biological samples and for materials with the risk of activation and heating.
- (iii) Acceleration of scan time to better monitor microstructural changes especially during fast cooling rate experiments.

CHAPTER II: STATE OF THE ART

Principles of X-ray Tomography

Radiation interaction with a material can cause atomic or molecular excitation, activation of the nucleus or ionization. Owing to their wave nature, no charge and mass, X-rays can penetrate materials over great thickness before undergoing any interaction. This makes them of interest in the field of tomography. The interaction of these electromagnetic waves with matter can occur in three ways: Pair production, photoelectric effect, and Compton scattering.



$$\frac{I_1}{I_0} = \exp(-\mu t)$$

$$\mu_{Photo} \propto \frac{\rho Z^n}{E^3}$$

$$\mu_{Compton} \propto \frac{\rho}{E^{0.3}}$$

Figure 3: Typical attenuation curve for Nickel showing various interaction mechanisms as a function of x-ray beam energy.

At low to medium energies, photoelectric effect is the most dominant attenuation mechanism. The total/linear attenuation coefficient (μ) of a material is the probability of the radiation beam interacting with the material while passing through it. The exponential decay of the radiation intensity as it passes through the material, as shown in Figure 4 below, is described by the Beer-Lambert's law.

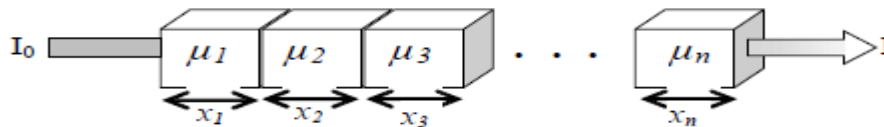


Figure 4: Attenuation of a radiation as it passes through a material [6]

$$I = I_0 e^{-(\mu_1 x_1 + \mu_2 x_2 + \mu_3 x_3 + \dots + \mu_n x_n)} \text{ where } \mu_1 x_1 + \mu_2 x_2 + \mu_3 x_3 + \dots + \mu_n x_n = \sum_1^n \mu_n \cdot x_n \quad (1)$$

$$\text{Hence } \sum_1^n \mu_n \cdot x_n = \ln \frac{I_0}{I} \quad (2)$$

In Equation 1, I is the final intensity of the radiation after passing through the material. μ is the linear attenuation coefficient, and x is the distance travelled by the radiation. The ratio $\ln \frac{I_0}{I}$ is the one-dimensional projection of the body in the direction of the x-rays.

In computed tomography, a series of projections are recorded as the sample rotates around the radiation source – detector axis, resulting from rays passing through the same section in the object. The exit beam intensity integrated along a line between source and detector is the process of reconstructing the images. Thus, the line integral of the linear attenuation coefficient is the basic measurement of computed tomography.

Image Reconstruction:

After multiple 2D projection images of the scanned object are acquired, a tomographic reconstruction algorithm is used to compute the 3D image of the scanned object's internal structure using all or some of the projection images.

Image reconstruction is the mathematical process used to generate tomographic images from the acquired x-ray projections. The process uses an algorithm which builds up image information from the attenuation data measured by the detector. The algorithm basically converts the attenuation coefficient values to maps of intensity and location within the object hence forming a greyscale image of the object.

Reconstruction algorithms can be broadly classified into two groups [7]:

1. Direct Algorithms: e.g., Filtered Back Projection (FBP)
2. Iterative Algorithms: Simultaneous Iterative Reconstruction Technique (SIRT) and Total-Variation minimization

Studies have concluded that direct algorithms like FBP are computationally efficient and can make accurate reconstructions if presented with many projections with little noise [8] [4]. Iterative algorithms on the other hand can produce better reconstructions than direct algorithms by taking advantage of prior knowledge of the scanned object and the setup of the experiment, with the drawback of high computational cost [9].

Convolutional Neural Network algorithm

In recent times, there has been increasing application of deep learning [10] [11] [12] to image processing in order to improve reconstruction accuracy from limited data. Deep learning has been used to improve images computed by direct algorithms. These algorithms have been employed in post-processing operations such as denoising and semantic segmentation. [13]

The approach is stated as follows:

$$x_{ML} = ML(x_{FBP}) = ML(A^T C_h y) \quad (3)$$

Where $ML: \mathbb{R}^{N \times N} \rightarrow \mathbb{R}^{N \times N}$ stands for the machine learning algorithm used to produce an improved image reconstruction from FBP images.

Deep Convolutional Neural Networks (CNNs) are a class of machine learning algorithms which work by successively processing images in layers, each layer made up of multiple images [4, 10]

The different layers learn to detect different features of an object. To compute the images of each layer, a process called convolution is introduced. During convolution, an image is transformed by applying a kernel/filter across the image pixel-wise. The kernel is a matrix whose elements and dimension determines the transformation effect of the process [14]. The convolution process is through the following steps: (1) The kernel is placed over each pixel of the image, with the full kernel within the image, and multiplies each value of the matrix with the corresponding pixel it is over. (2) The resulting product of the multiplies values are summed, and returned as the new value of the center pixel. (3) The process is repeated pixel-wise across the entire image [15]. CNNs convolve images of a previous layer with learned filters and apply a non-linear activation function to each pixel of the resulting image.

For a certain Image j in layer i of the network represented as $z_i^j \in \mathbb{R}^{N \times N}$, and the total number of images in layer i represented as n_i , the mathematical representation of the computation of z_i^j in a Convolutional Neural Network is:

$$z_i^j = \sigma \left(\sum_{k=0}^{n_{i-1}-1} H_{q_{ijk}} z_{i-1}^k + b_{ij} \right) \quad (4)$$

Where;

$H_{q_{ijk}}$ is a 2D convolution with a learned 3 x 3-pixel filter $q_{ijk} \in \mathbb{R}^{3 \times 3}$

b_{ij} is a learned bias of each layer image

$\sigma: \mathbb{R}^{N \times N} \rightarrow \mathbb{R}^{N \times N}$ is a non-linear pixel-wise activation function e.g., the ReLU function

Convolutional Neural Networks typically employ supervised learning to find values for the trainable parameters q_{ijk} and b_{ij} . Supervised learning involves the use of a large set of training image pairs, each pair made up of an input and a matching target image which represents the ideal network output for that image. Following the random initialization of the network parameters, the training images are used to iteratively minimize an objective function that computes the error between the network output and target images. For most CNNs, the use of the encoder-decoder network architecture and the additional operations introduced in the processing, present some application complexity due to the large number of training images required. Also, there is the need to copy image features found in a certain layer into subsequent layers in order to be used. The encoder part and the decoder part are somewhat separated hence information learned by the decoder part cannot be used by the encoder part.

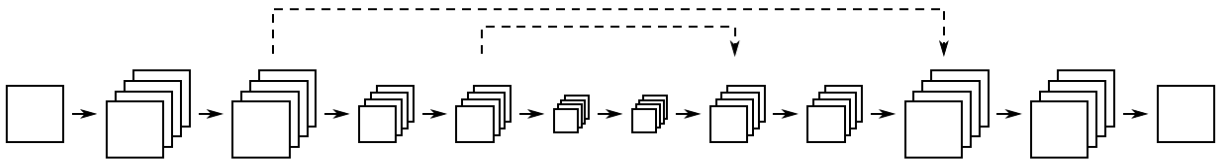


Figure 5: Graphic representation of typical encoder–decoder CNN. The input image is shown on the far left and the network output on the far right. In the middle are the multiple layers, with arrows depicting convolutional operations, downscaling operations, and upscaling operations between layers. Skip connections are depicted by dashed arrows [4].

Mixed-Scale Dense Convolutional Neural Network (M-SDNet) Algorithm

The Mixed-Scale Dense Convolutional Neural Network (M-SDNet) algorithm is a reconstruction algorithm in which a machine learning component is introduced. In this algorithm, there is optimization of some of the algorithm parameters through supervised learning. By adding a machine learning component, reconstruction accuracy is improved while maintaining computational efficiency [12]. This algorithm improves the image quality of direct methods for data with limitations (e.g., data with noise or a low number of projection angles). The algorithm uses less training parameters than other convolutional neural network algorithms to produce high quality images. M-SDNet avoids some of the limitations of the encoder-decoder CNNs by having all layers densely connected, meaning that all previous layer images are utilized to compute the image of a certain layer.

M-SD Networks do not incorporate intermediate image layers but rather use dilated convolutions to capture image features at various scales. With each layer having a specific dilation, each layer captures features at a certain image scale. This approach mixes the encoder and decoder parts by choosing certain dilation distribution thus allowing information from uses across the network.

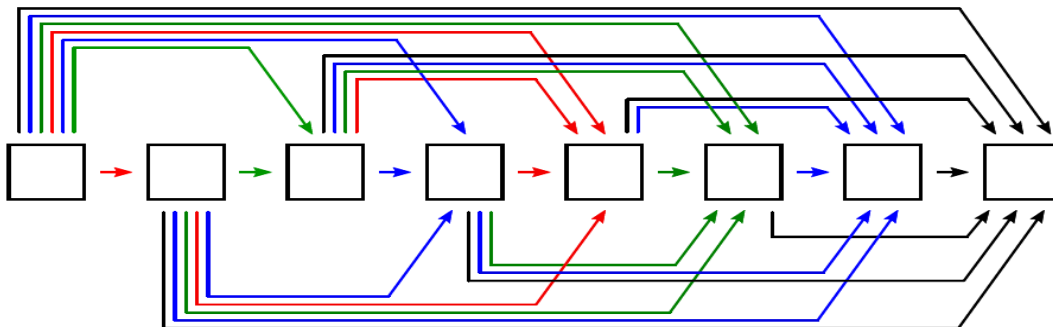


Figure 6: Schematic of an M-SD network. Arrows depict dilated convolution operations, with each colour representing a different dilation factor. Note that all intermediate images are the same size, all layers consist of only a single image, and each layer (including the output layer) takes all previous layer images as input (including the input image). [4]

A number of researchers have highlighted the advantage of M-SDNet algorithm over other CNNs. Pelt et al [5] compared the segmentation accuracy of M-SDNet and other CNNs using U-Net architecture, for very large files with complex features. The result shown in Figure indicates that with over 60 training iterations, the M-SDNet architecture returned close to 90% global accuracy compared to about 80% for the U-Net algorithm. Also, the segmentation from the M-SDNet closely matched the manual segmentation of the volume considered.

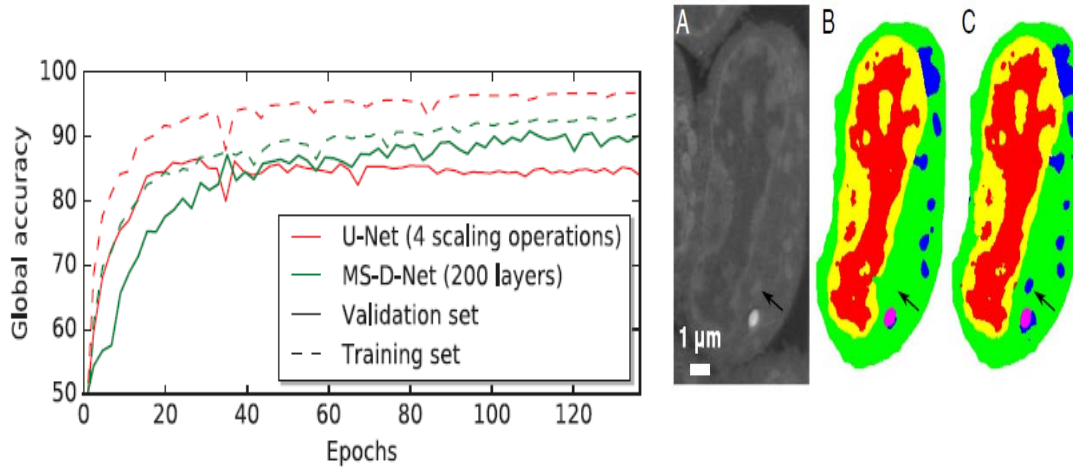


Figure 7: The global accuracy of a U-Net network and an MS-D network as a function of the training epoch (left). (A–C) A tomographic slice of the test cell (A), with the corresponding manual segmentation (B) and output of an MS-D network with 100 layers (C). [5]

Reconstructions with limited number of projections using M-SDNet, the classical FBP, and a neural network-FBP showed that the M-SDNet algorithm returned better quality metrics as concluded in [4] [16]. The MS-D network output yielded significantly better accuracy than the other algorithms as shown in Figure. The NN-FBP reconstructions were more accurate than the FBP, but lagged the M-SDNet output because the neural network underlying the NN-FBP algorithm had a single layer limiting its ability to learn from highly non-linear features.

It can be concluded from literature that typically; deeper networks produce outputs with better accuracy results than shallower networks. As a result of the dense connections in MS-D networks, networks with many layers and fewer channels per layer can be effectively used, thus yielding very deep networks with relatively few channels.

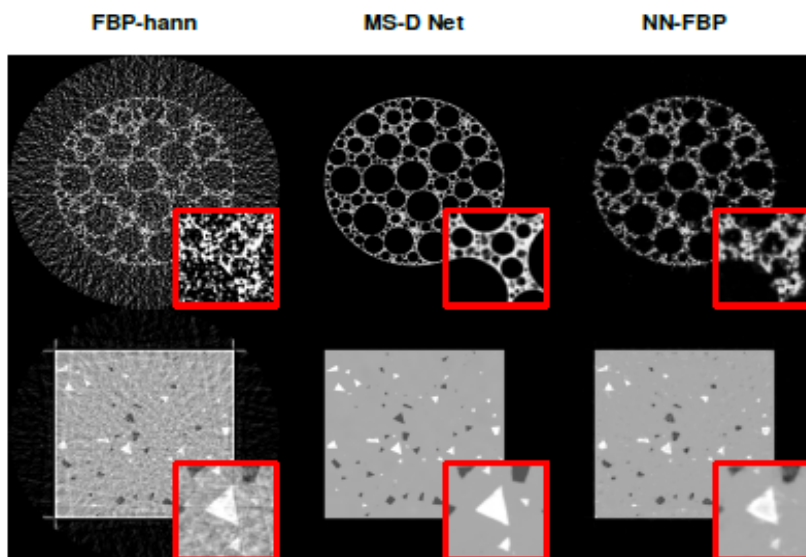
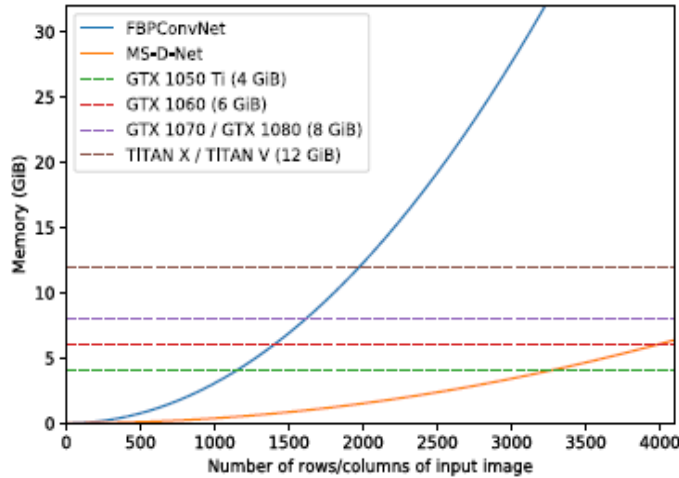


Figure 8: Reconstructions from 32 noise-free projections, using FBP with the hann filter, the proposed MS-D network, and the NN-FBP algorithm. [4]

As a result of the dense architecture of M-SDNet and the relatively fewer training parameters needed, the computer storage space needed for the network is significantly reduced compared to other algorithms. This has been demonstrated by D. Pelt et al in [4].



From Figure on the left, as the pixel sizes of the input images increase, the FBPConvNet require significantly more memory space than M-SDNet which would need slightly more than 5GB of memory for very large input images, typically obtained during synchrotron and lab x-ray tomography.

Figure 9: The required memory to store all intermediate images of a FBPCovNet network and a MS-D network with 100 layers as a function of the size of the input image, shown with the maximum usable memory of several NVIDIA GPUs. [4]

Image Comparison

To quantitatively compare images, some metrics have been developed which take into account the distortions in the image itself or with respect to a certain ‘reference’ image. These objective image quality metrics are useful, especially to optimise algorithms hence the output of image processing systems. Some of these metrics include; mean squared error (MSE), the peak signal-to-noise ratio (PSNR), the structural similarity index (SSIM) [17]etc.

The Structural Similarity Index (SSIM) compares two images based on three features; Luminance, Contrast and Structure [18]. See Figure 7 for a schematic of the measurement. This value varies between 0 and 1, with 1 meaning very similar and 0 indicating very different.

Luminance is calculated by taking an average over all the pixel values in the image. For two image signals x and y ;

$$\text{Luminance, } \mu_x = \frac{1}{N} \sum_{i=1}^N x_i \quad (5)$$

Contrast is calculated by taking the square root of the variance of all pixel values

$$\text{Contrast, } \sigma_x = \left(\frac{1}{N-1} \sum_{i=1}^N (x_i - \mu_x)^2 \right)^{1/2} \quad (6)$$

Structure is calculated by dividing the input signal with its standard deviation, to obtain a normalized signal.

$$\text{Structure } s(x) = (x - \mu_x / \sigma_x) \quad (7)$$

Combining these three components with some mathematical rigour, expressed in [10], the SSIM is thus:

$$SSIM(x,y) = \frac{(2\mu_x\mu_y + C_1)(2\sigma_x\sigma_y + C_2)}{(\sigma_x^2 + \sigma_y^2 + C_2)(\mu_x^2 + \mu_y^2 + C_1)} \quad (8)$$

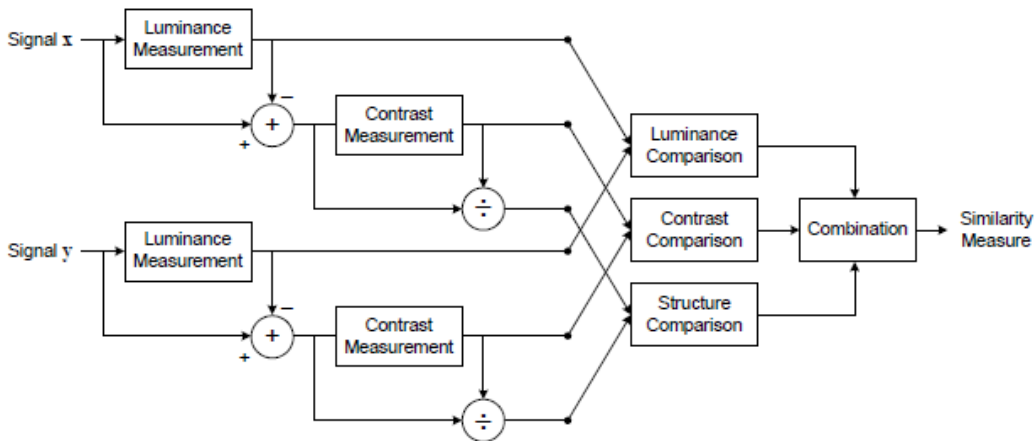


Figure 10: Schematic of the measurement system for Structural Similarity Index [18]

The Mean Squared Error (MSE) is the square of the mean of the error between the reference and the other image, estimated pixel by pixel in both images.

MSE is given by:

$$MSE = \frac{1}{M*N} \sum_{i=0}^{M-1} \sum_{j=0}^{N-1} [I(i,j) - K(i,j)]^2 \quad (9)$$

$K(i,j)$ is the reference image with dimensions M and N, while $I(i,j)$ is the other image. i and j are the row and column pixels of both images. The value of MSE varies between 0 and 1, with identical images having a MSE of 0.

Peak Signal-to-Noise Ratio (PSNR) represents the ratio between the maximum possible power and the corrupting noise affecting the image representation.

PSNR is related to the MSE by the relation below.

$$PSNR = -10 \log_{10} MSE \quad (10)$$

The objectives of this study as explained in the Context chapter is to investigate the use of the M-SDNet algorithm, a neural network algorithm, in the improvement of image reconstruction especially for in-situ tomography where the constraints of scan time and resolution, present a huge challenge with the use of classical reconstruction algorithms requiring a large number of projections to make accurate reconstructions.

While some researchers have investigated the application of the M-SDNet algorithm for reconstruction using limited data, literature shows that detailed quantitative study of features (especially cavities) has not been carried out. This study adds to existing knowledge while taking a step further into quantitative analysis of cavities in reconstructed images from FBP, SIRT and the novel M-SDNet algorithm. In the Materials and Methods chapter, detailed description of the materials, algorithms and approaches used are given. Results of experiments carried out are discussed and comparison of the M-SDNet results with classical algorithms are presented. Finally, perspectives on future research are given.

CHAPTER III: MATERIALS AND METHODS

Al-Cu-Si Scanned at ESRF:

Two samples, sample 1 and sample 2, obtained from the solidification experiment of an Aluminium alloy: Al-Cu-Si, were studied in the course of this project. The sample images were obtained from scanning an in-situ high cooling rate solidification experiment at the European Synchrotron Radiation Facility (ESRF) on ID19 beamline in 2018.

50 scans were taken of the sample following the cooling of the sample from pure liquid state into the two-phase zone, marked red in the generic Al-Cu-Si phase diagram in Fig. below.

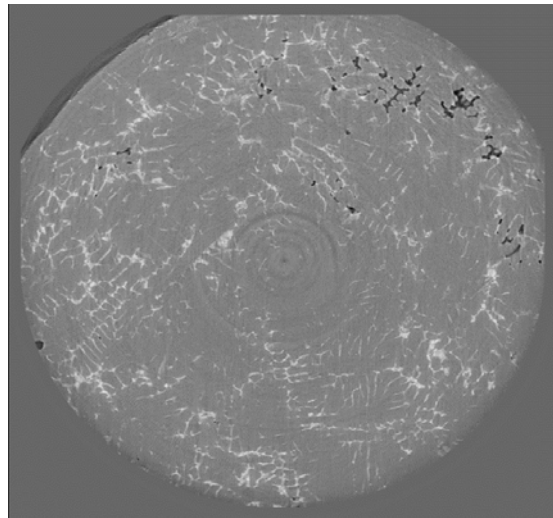


Figure 11: 2D slice of a high-resolution scan of Al-Cu-Si sample made at the ESRF.

Sample 1 and Sample 2 are similar except for the amount of hydrogen present in Sample 1 is smaller. Table 1 summarizes the scan conditions of the samples.

Table1: Scan condition of the Al-Cu-Si solidification at ESRF. Composition Al 8wt%Si 3wt%Cu

Scan Condition	
Pixel size	1.1 μ m
Number of projections	500
Scan time	0.3s
Exposure	0.006s/projection
Field of view (FOV)	1008 x 1008 x 1008 (however we reduced to 226 projections)

The sample image shown in Fig. shows the different phases in present after the solidification of the sample: Al rich phase in grey, intermetallic phase (eutectics) in white, and cavities in black. The cavities have been chosen as the focus of this study as the benchmark to quantitatively analyse the effect of the chosen reconstruction algorithm in improving aspects of the image reconstruction.

316L(N) Steel

We also investigate a 316L(N) alloy used in the PhD of Oguz Ozdemir: this alloy is meant to be used in Fast nuclear reactors such as the one investigated in GENIV reactors. The composition of the alloy is given in table 2. The sample has been submitted to creep tests at 550°C under 340Mpa up to rupture which happens after 20221 hours, i.e., long time creep.

The high-resolution scans were performed at the European Synchrotron radiation facility (ESRF) on beamline BM05, at a pixel size of 1.35µm leading to a spatial resolution of about 2.7µm. The mean energy was set to 100keV in auto attenuation mode with 0.1mm of Mo. The detector was a PCO Edge camera (FOI of 2048 x 2048) with LuAg 100 scintillator. 2500 projections were taken over 360° in local tomography. The exposure time for each projection was 0.1s, and 4 projections in accumulation mode were taken, leading to a total scan time of 1000s. 3D volumes were reconstructed using PyHST from ESRF with the Paganin reconstruction method taking a value of alpha over beta of 500 and using only 1250 projections over 180°

Table 2: Composition of crept 316L(N) steel sample used for study.

Designation	C	Si	Mn	P	S	Cr	Ni	Cu	Mo	Co	B	N	Nb
RCC-MR _x 2018	≤0.03	≤0.5	1.60 2.00	≤0.03	≤0.015	17.00 18.00	12.00 12.50	≤1.00	2.30 2.70	<0.2	≤20 ppm	0.06 0.08	-
LN Sample	0.03	0.39	1.84	0.028	<0.003	17.3	12.5	0.17	2.48	0.13	11	0.075	0.014
HN Sample	0.021	0.42	1.71	0.021	0.0018	17.7	12.6	0.06	2.46	0.03	19	0.1	0.09

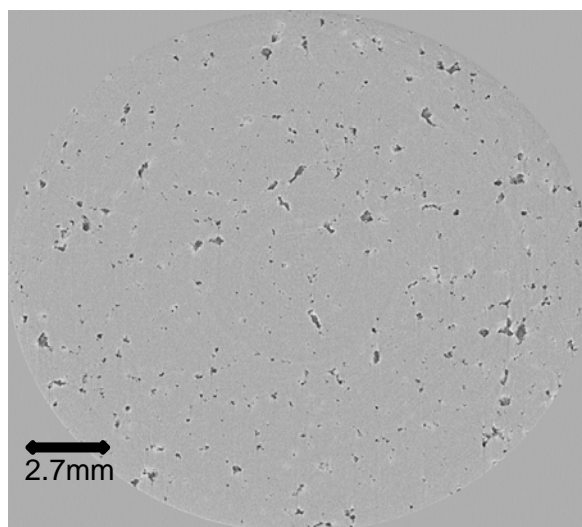


Figure 12: Scanned volume of 316LN steel sample

Al-Cu-Si Laboratory Tomography

Sample1 of the Al-Cu-Si alloy was also experimentally analysed at different resolutions using EASYTOM XL tomography with a laboratory x-ray source. The image on the left in Fig. 9 is the EASYTOM XL laboratory tomograph used for the experiment. The principle of operation is explained in image on the right: the specimen is exposed to a cone beam x-ray source and the beam of x-rays attenuated by the sample is measured with a detector on the other side. The sample slowly turns in step-wise circular motion, in different angles, until the full 3D volume is reconstructed.

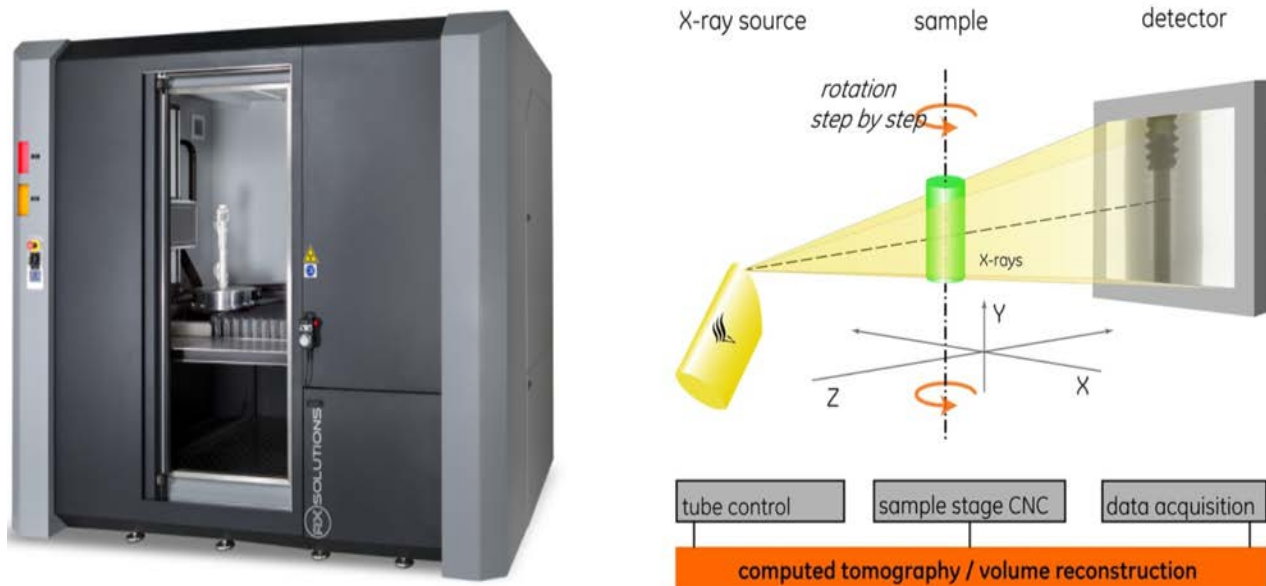


Figure 13: (a) Easytom XL X-ray tomograph machine (b) schematical illustration of the working principle.

The sample was scanned at high resolution of $1\mu\text{m}$ while varying the number of projections, the number of frames used to average an image for a scan, and at 1 frame per second. A second batch of scans were made at a resolution of $1.5\mu\text{m}$, varying the number of projections, the frame rate and the average number of frames. Scans were made in continuous mode and in stepwise mode to also understand the effect on the image quality.

Finally, tomographs were acquired in conditions similar to in-situ experimental conditions. The Source-to-Sample Distance (SSD) was adjusted to accommodate a furnace, while the Source-to-Detector Distance (SDD) was adjusted to obtain the best resolution possible. Scans were made in these conditions while also varying the number of projections, frame rate and average number of frames. All the scans were made at 70kV and $66\mu\text{A}$ with an Al filter placed between source and object to selectively absorb low energy and wavelength photons to improve beam coherence.

Table 3 below summarises the different scans made on the sample with varying experimental conditions.

Resolution (μm)	Frame Rate (fps)	Average frames	No. of projections	SOD (mm)	SDD (mm)
<u>High resolution scan</u>					
1	1	5	1440	0.5	348
1	1	5	160	0.5	348
1	1	1	160	0.5	348
1	1	5	96	0.5	348
1.5	2	5	96	0.5	452
1.5	2	1	96	0.5	452
1.5	2	5	160	0.5	181.52
1.5	2	1	160	0.5	181.52
1.5	2	5	1440	0.5	181.52
<u>In-situ condition scan (continuous and step-wise scan)</u>					
4.32	4	1	96		
4.32	2	5	288		
3	2	1	288	15.4	654
2.5	1	1	288	12.9	654

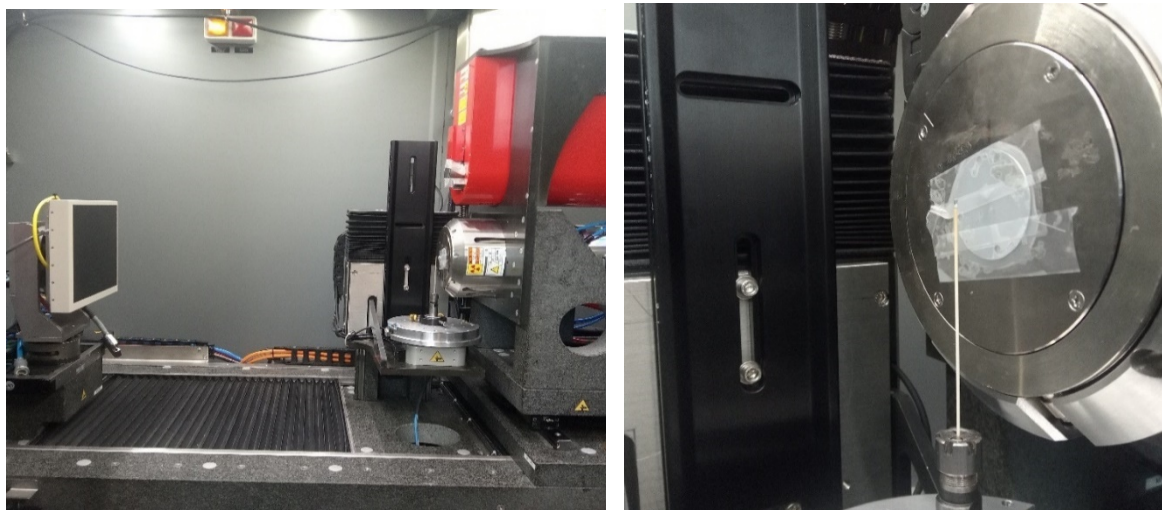


Figure 14: Experimental setup for lab tomography(left). Sample on a stand close to source (right)

The frame rate indicates how many images were captured per second. For high quality acquisitions, lower frame rates are used, however depending on the number of projections needed, a low frame rate will increase acquisition time and dose. For in-situ imaging, a high acquisition time is avoided because of the need to quickly follow the evolution of microstructure and properties of the sample. To reduced random noise in the image as a result of fluctuations in beam intensity, image averaging

is used. Generally, random noise decreases by the square root of the number of images averaged [19]

Image Processing

Image Reconstruction:

Al-Cu-Si sample projections obtained in the laboratory were reconstructed with Xact software of Rx Solutions, using the classical back-projection algorithm (FBP).

The ESRF scanned Al-Cu-Si sample was reconstructed with the Astra toolbox [20], implemented in Python, with standard toolbox parameters, using low number of projections: 500, 300, 200, 150, 75, 50. A SIRT reconstruction was also carried out in Astra toolbox using 70 iterations and standard parameters for SIRT reconstruction.

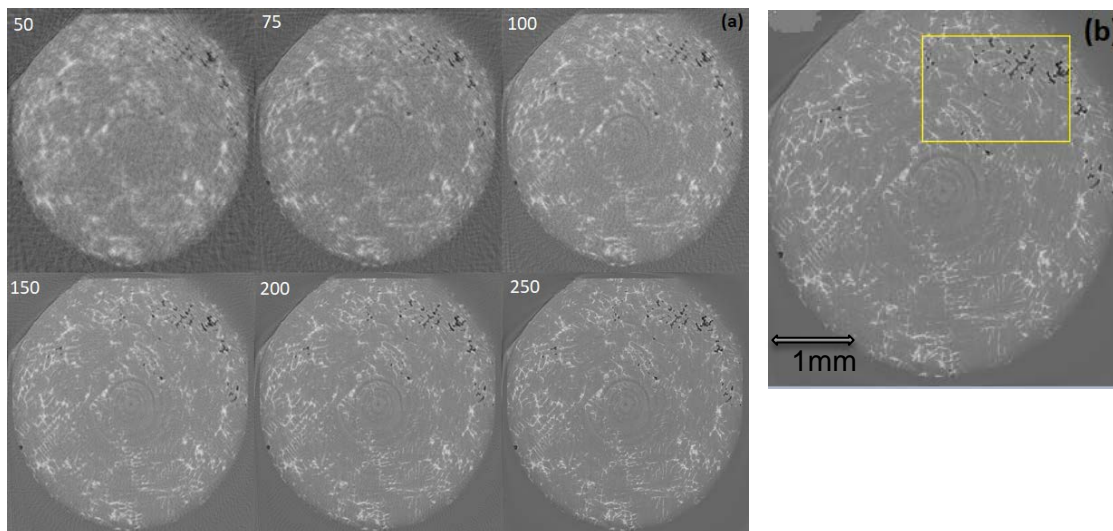
The low number projections reconstructions of the 316L(N) sample were reconstructed using an FBP reconstruction algorithm in the Astra toolbox, implemented in Python, with various number of projections; 50, 75, 100, 150, 200, 300, 500.

The Al-Cu-Si alloy FBP reconstructed images were reconstructed also with the M-SDNet algorithm, taking the 500 FBP projection reconstruction as target. This would be referred to as AI images throughout the course of this report.

Zone Selection:

A zone of study/region of interest (ROI) was selected on the Al-Cu-Si volumes obtained from using different projections. The small zone selected, shown in Fig. 15(b) has cavities with various sizes.

The small zone selected corresponds to a field of view (FOV) of 467 x 307 x 225. This is shown in Figure 15(a), (b) and (c).



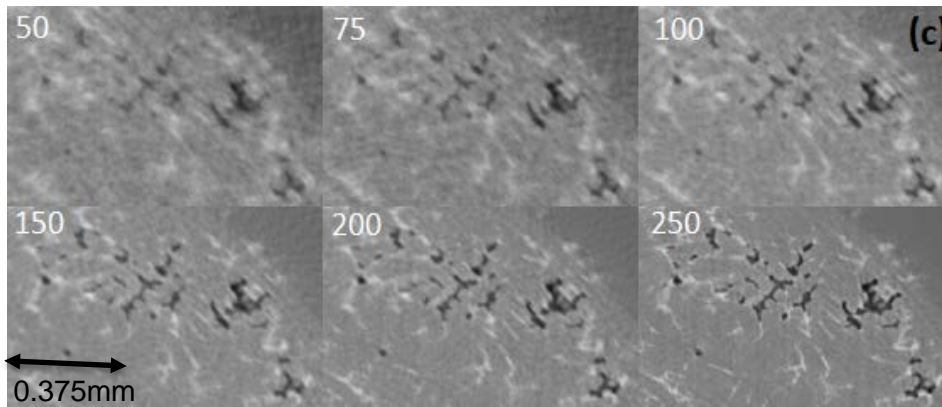


Figure 15: (a) 2D slices of low number projection of FBP reconstructions of Al-Cu-Si sample. (b) Region of interest marked in a yellow rectangle (c) Cropped zone with various sizes of cavities

A qualitative comparison of the 2D images in Fig. 15(a) show decreasing noise as the number of projections increased. For the cropped region of interest, image features become more prominently reconstructed from 50 projections to 250 projections. Small cavities were lost in reconstruction with 50, 75 and 100 projections. As a consequence, improving reconstruction accuracy with the proposed neural network algorithm should reconstruct images features while reducing as much as possible, with minimal number of projections.

The 316L(N) images are shown in Figure 16 below.

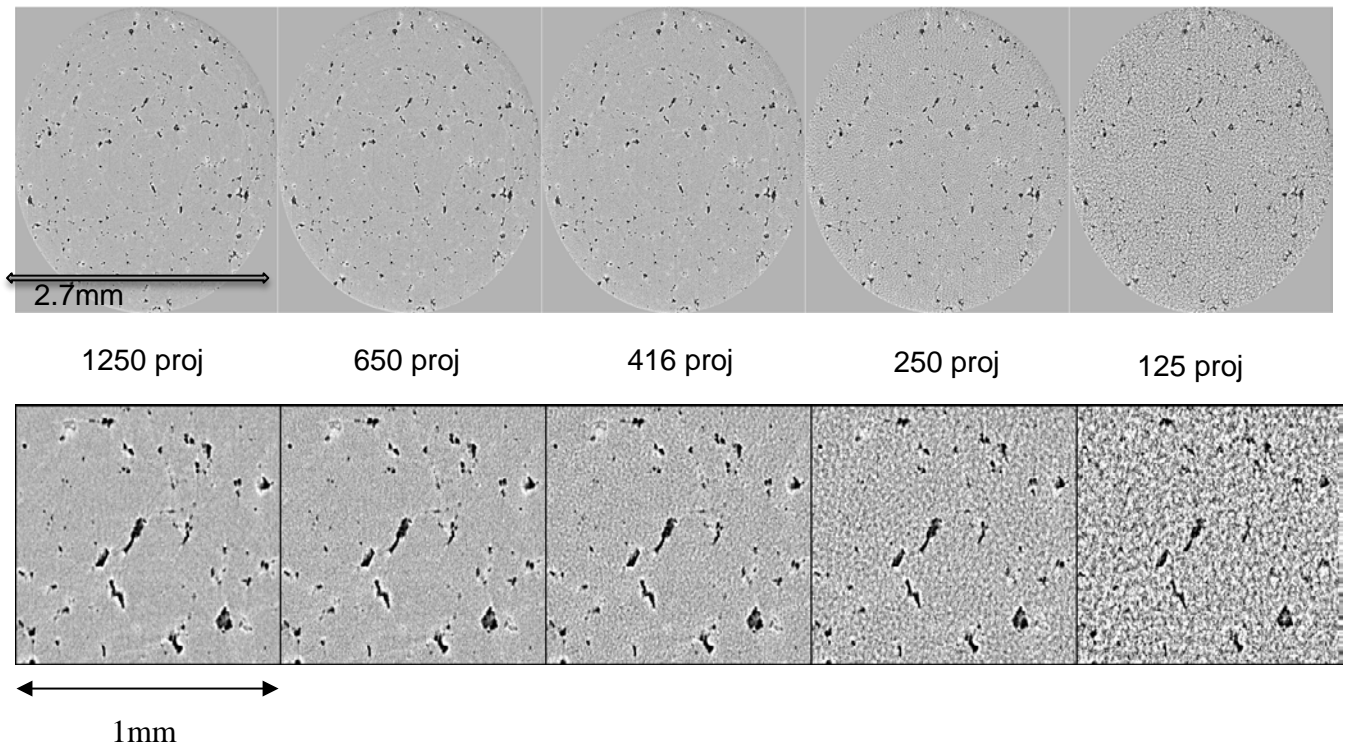


Figure 16: Low number projection of FBP reconstruction of 316L(N) (top). Cropped region of Interest (bottom).

The FBP reconstruction of the 316L(N) projections had increased background noise as the number of projections reduced down to 1/10 of the high-quality reference image (1250 projections). The white phase was also increasingly difficult to differentiate. With the M-SDNet algorithm, it is expected that we gain at least a factor of 5 for accurate reconstruction of the projection images i.e. using 250 projections to obtain a relatively similar volume as the high-quality volume.

Image Filtering

Image filtering is the first step in the image processing segment of the methodology. It involves the methods for image enhancement and noise reduction in order to differentiate the different features in the image. Different modes of filtering; Median filtering, brightness and contrast, gaussian filtering, anisotropic diffusion 2D filter etc., implemented in *ImageJ* as plugins, were applied to the images in various ways and extents to reduce the noise and enhance the images.

Segmentation

The segmentation step involves separating the "regions of interest" from the "background" of an image. The result of this step is a two-level or "binary" image, consisting of pixels in one of two states: pixels in regions of interest or background. Segmentation of the cavities was achieved through thresholding; specifying a grey level tone for cavities above which values are considered white and below which they are considered dark. Cavities/porosities were represented as white objects while the intermetallic and primary phase are lumped into the black background. Image processing for all the samples analysed was performed with *ImageJ* [21].

Parameter Analysis:

Quantitative analysis of each volume was carried out using parameters obtained from the different segmentation threshold values using the Analysis 3D plugin developed at SIMaP, Grenoble [22] in *ImageJ*. Features taken into account had volume greater than 8 voxels.

The volume fraction of cavities (pores), number of cavities and 3-D rendering of the cavities were obtained using Python and the python-based toolbox, Mayavi [23]. We also investigate local information on each pore such as volume and sphericity to perform full quantitative comparison of IA reconstructed volumes to FBP reconstructed volumes.

Data Comparison

To compare the various grey-level images obtained using the different reconstruction algorithms, some general metrics were used to obtain values which related each image to a reference high quality image. The general metrics used included; Structural Similarity Index (SSIM), Mean Squared Error (MSE) and Peak Signal-to-Noise Ratio (PSNR). These metrics were calculated on Python using embedded routines in the Skimage toolbox. [24]

Automatic Cavity Tracking

Particles (cavities) were manually tracked across Reference and analysed volumes to compare their properties, establish quantitative comparison, and judge the effectiveness of reconstruction algorithms in reproducing features based on the number of projections used. This was done by making a global sphericity-volume curve of all particles in all the volumes using the result output file (res.dat) from parameter analysis in the Analysis 3D plugin of *ImageJ*. Different regions of

volume and sphericity on the curve were selected, and then corresponding cavities were manually tracked and compared.

A follow-up procedure was an automatic particle tracking routine implemented in python to match the spatial position of cavities found in the Reference volume with similar cavities in the analysed volumes, using their centres of gravity. A minimum error in distance between the centres of gravity of identical particles in Reference and Analysed volume was set as a matching criterion. Objects which matched in both Reference and Analysed volumes were collected, represented in 3D using Mayavi, and compared based on cavity properties – sphericity and volume. An error-volume plot was made to observe variations in the matching procedure as a function of the volume of cavities.

The algorithm of the automatic procedure is shown in Table below:

Table 4: Algorithm implemented in python for particle tracking.

Algorithm for automatic particle tracking:	
1.	Load data files for all volumes, and assign variables to Ref and IA volumes
2.	Read cavity parameters from input data; sphericity, volume, center of gravity coordinates, and surface area, and set to update after calculation.
3.	Create an output file for each required output parameter; volume, sphericity and dv, the distance between center of gravity of Ref and IA volumes, to store the required parameters and put zeros when pore is not found in IA
4.	Set range and limits on dv.
5.	Calculate the distance between center of gravity of Ref and IA volume, and update output file if limit condition is met.
6.	Calculate and plot the relative error in dv as a function of cavity volume.
7.	Make a 3D rendering of cavities with Mayavi, and combine matching cavities in a single plot.

M-SDNet Application

The strategies adopted in the methodology of this project is summarized in the flow chart Figure below. They correspond to the two categories of algorithms in the M-SDNet suit, namely;

- Regression algorithm – for denoising grey-level input images with grey-level target images.
- Segmentation algorithm – for segmenting grey-level input images with binary target images.

The methodologies include;

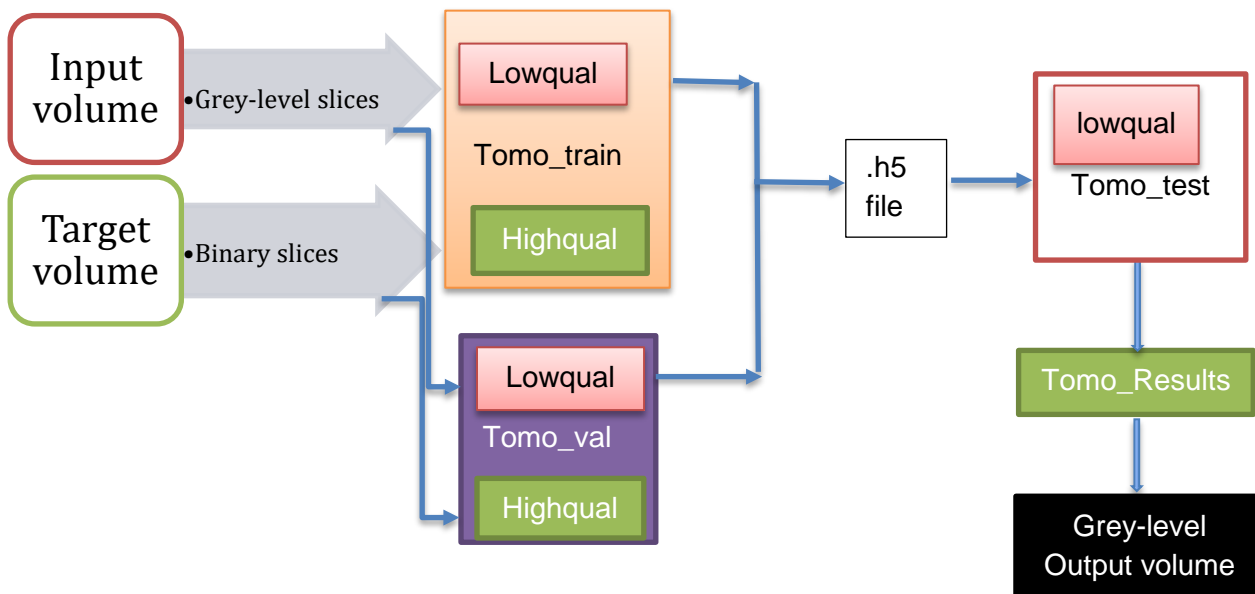
- 1) Training with target and input images as grey-level images.
- 2) Training with high quality segmented images as target and grey-level images as input

In each of the cases, the output volumes were then quantitatively analysed focusing on cavities and cavity properties.

‘Tomo_train’ folder contains the training dataset divided into ‘lowqual’ and ‘highqual’ folders, containing slices of the input and target images respectively. ‘Tomo_val’ is the validation folder with about 20% of the input and target images in ‘lowqual’ and ‘highqual’ folders. After the training, the network parameter (.h5 file) which encodes the variables controlling the training, is

applied to the test folder ‘Tomo_test’, containing the low-quality images to produce results stored in the ‘Tomp_results’ folder.

M-SDNet Segmentation Algorithm



M-SDNet Regression Algorithm

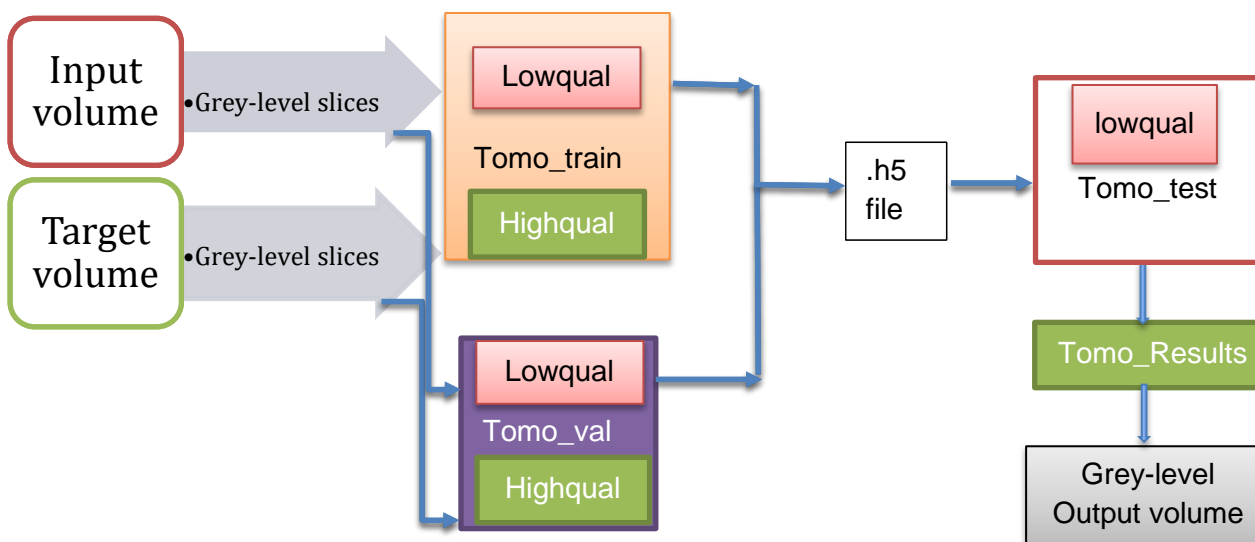


Figure 17: Two training strategies in the M-SDNet architecture.

CHAPTER IV: RESULTS AND DISCUSSION

Qualitative Inspection of grey level images

Figure 18 compares FBP and SIRT reconstruction as a function of the number of projections.

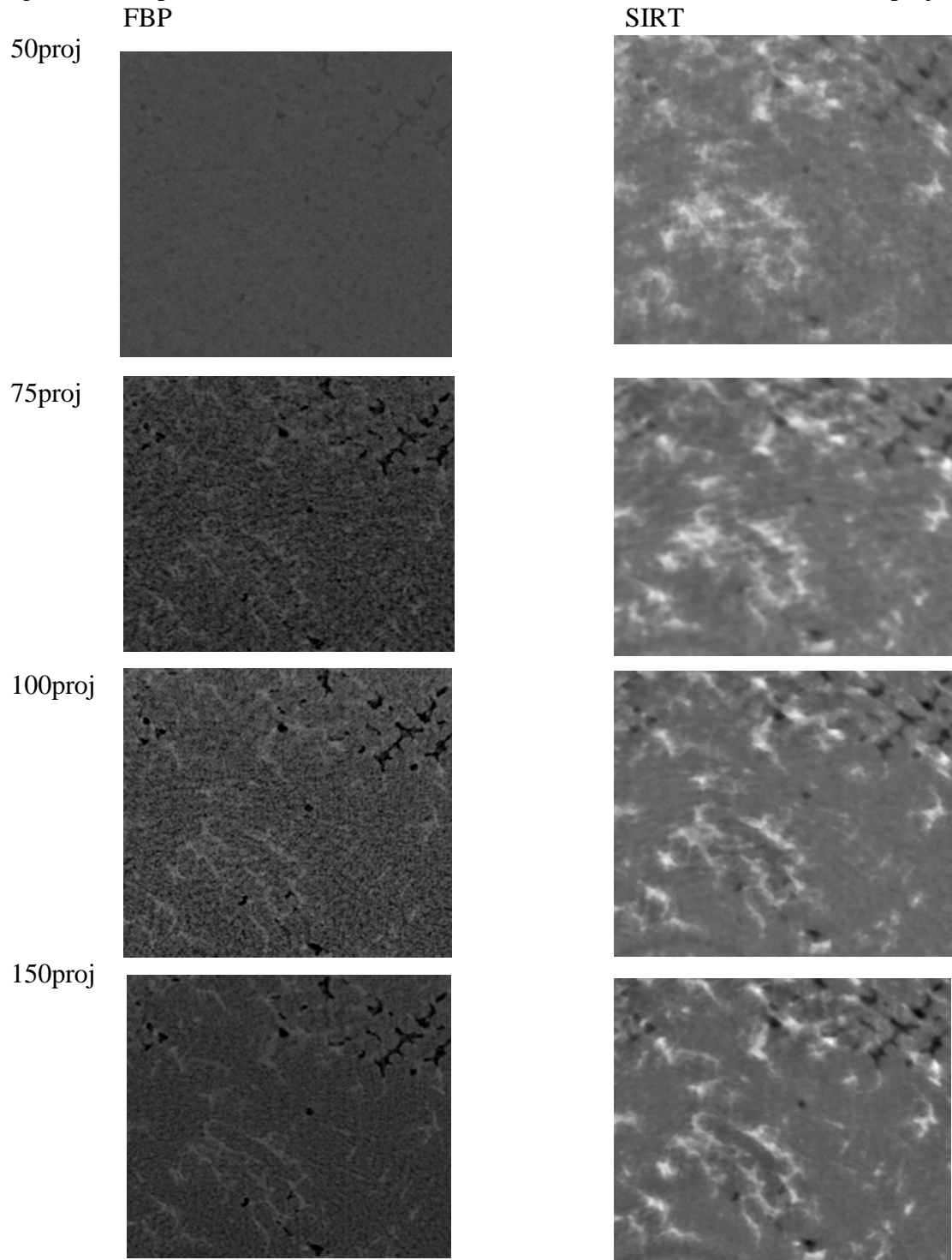


Figure 18: Qualitative comparison of FBP and SIRT reconstructed volumes for Al-Cu-Si sample

From Figure 18, the general trend is that the quality of reconstruction increases with the number of projections used. The FBP reconstruction showed less noise and reconstructed cavities better than the SIRT reconstruction.

Artificial Intelligence (IA) reconstructed volumes:

The grey-level IA volumes for the Al-Cu-Si sample reconstructed with the M-SDNet algorithm using low number FBP projections are shown in Figure 19 below.

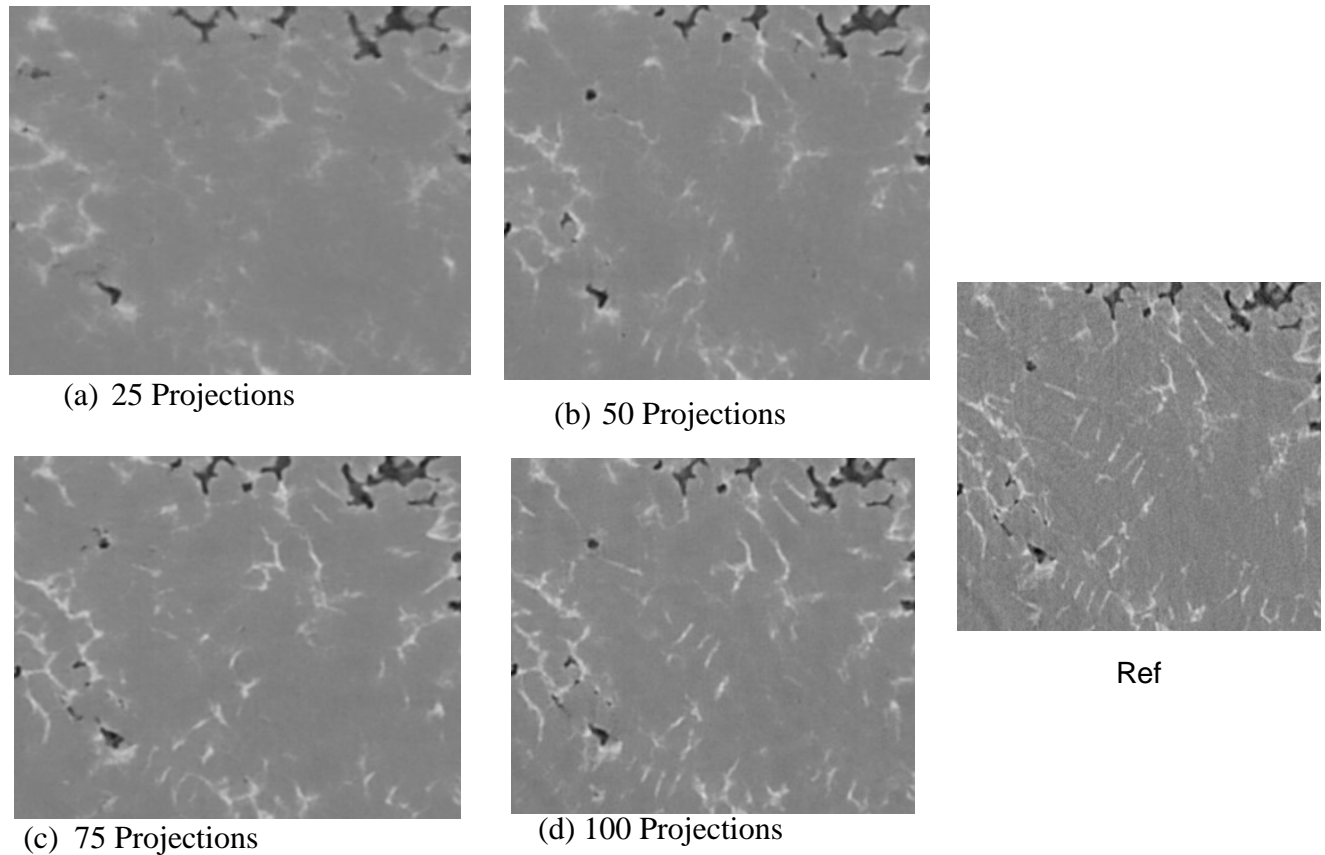


Figure 19: AI reconstructed volumes showing different projections

For the grey-level IA volumes shown above, the cavities were better reconstructed using 50 projections and above, when compared with the Ref. This is not the case if the focus is on the intermetallics which were not well represented between 25 projections to 75 projections. At least 100 projections would be needed for the intermetallics.

Qualitative Inspection of Binary Images:

Figure 20 compares binary FBP and SIRT volumes as a function of the number of projections.

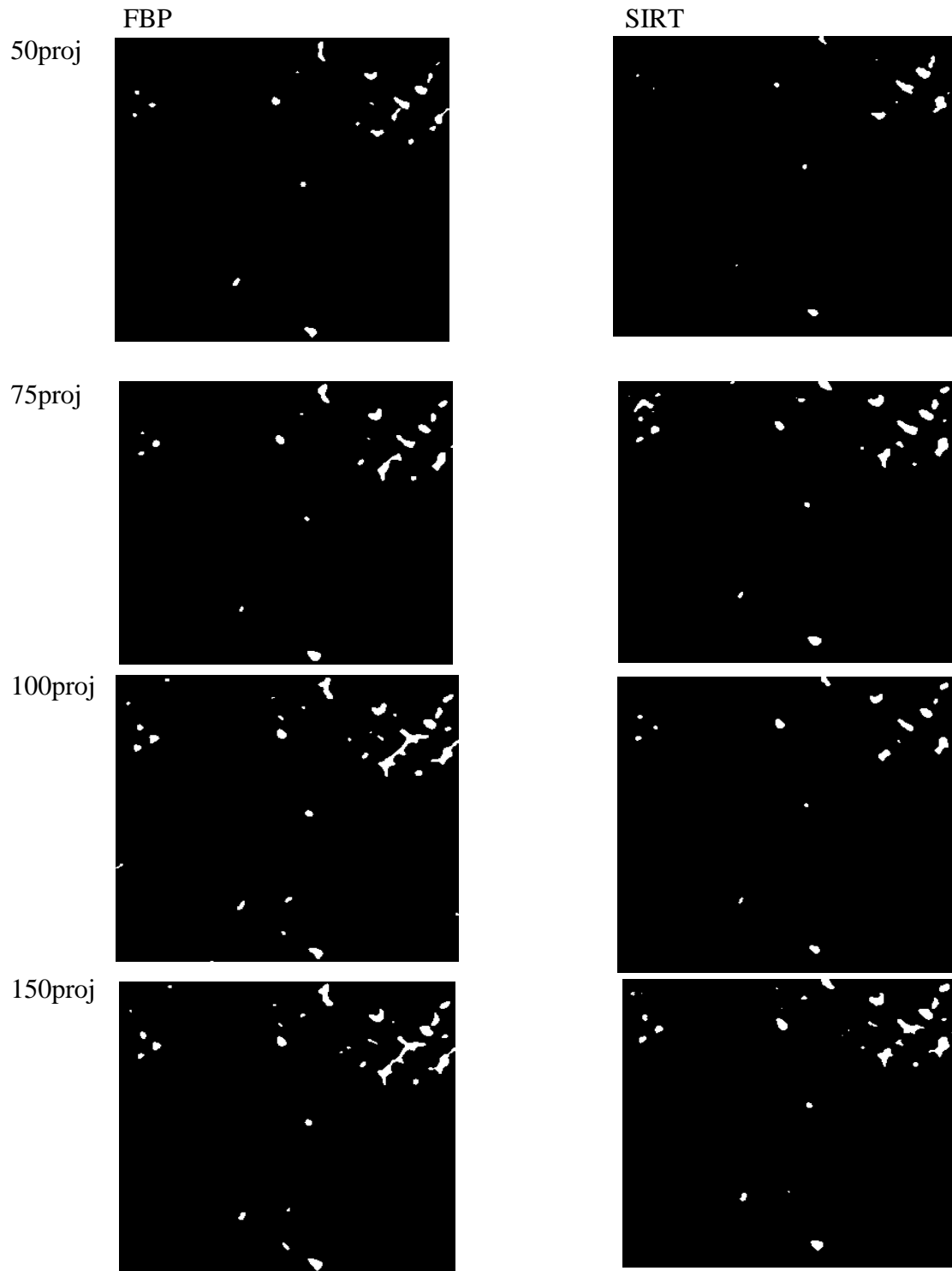


Figure 20: FBP binary volumes showing different projections

These images represent a binary image of the various FBP and SIRT volumes filtered, and segmented with a threshold value of 90. Qualitatively, it can be observed that the FBP images reconstructed the cavities much better than SIRT. Also, many small cavities were not captured in the SIRT reconstruction. The pixels of bigger cavity were discontinuous in the SIRT and as such a quantitative analysis of the number of cavities will show huge differences between SIRT and FBP across the different number of projections.

Artificial Intelligence Reconstructed Volumes:

The binary AI volumes segmented with *ImageJ* with a threshold value of 105 are shown in the Figure 21 below.

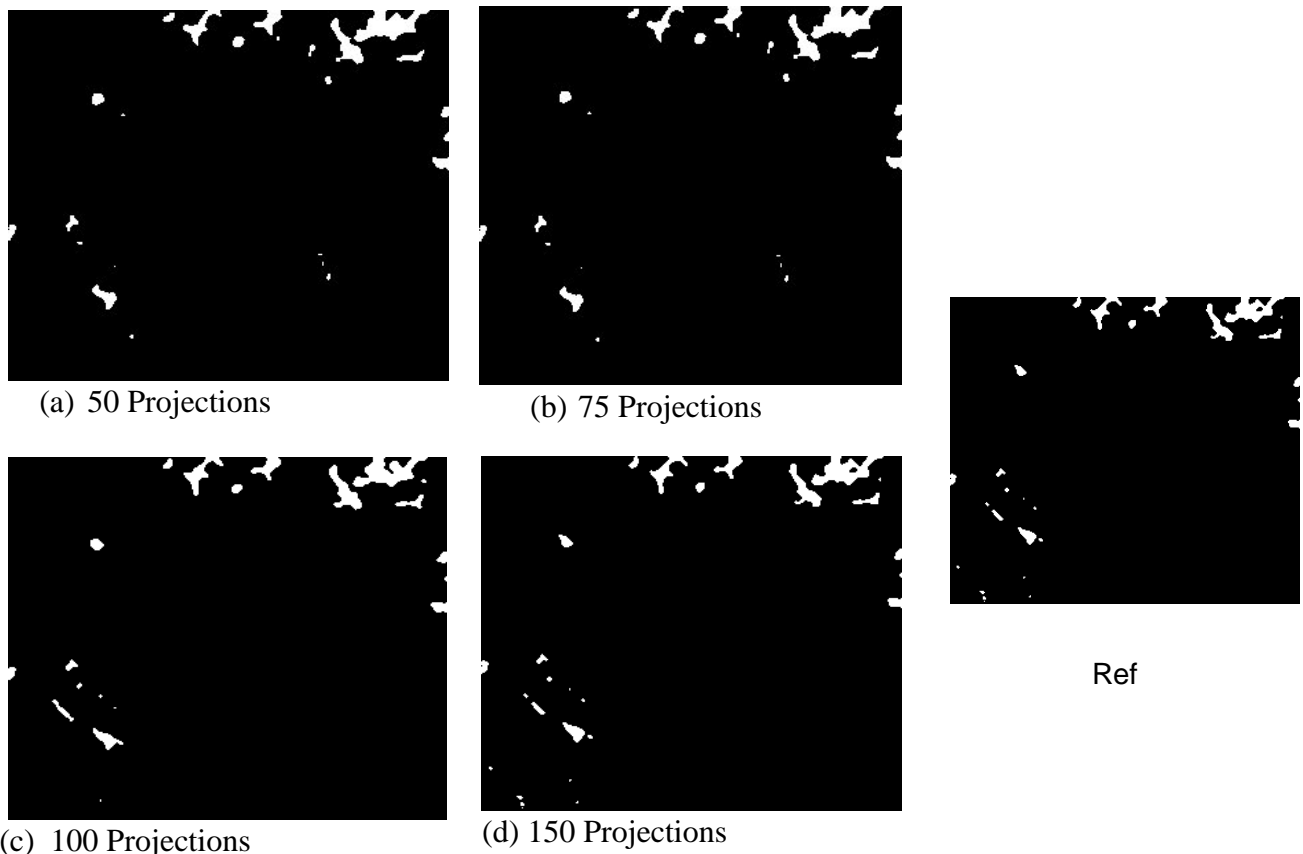


Figure 21: IA binary volumes showing different projections

The IA binary volumes shown in Figure 18 were segmented with a threshold value of 105. A qualitative comparison of the images shows minimal differences in across volumes. As the number of projections increased, the number of cavities observed become match that of the Ref volume. The neural network reconstruction with 150 projections is significantly same as the Ref – an FBP reconstruction with 500 projections. This shows that with M-SDNet, a limited number of projections can accurately reconstruct high quality images. Here we see a gain of a factor of 3.

Quantitative Comparison of IA Reconstructed Volumes:

General Metrics:

The different volumes reconstructed with the Filtered Back-Projection (FBP), Simultaneous Iterative Reconstruction Technique (SIRT), and Artificial Intelligence algorithms were quantitatively analyzed. The metrics used for the comparison include; number and volume fraction of pores, pore parameters like sphericity and volume, as well as full reference metrics like Structural Similarity Index (SSIM), Mean Squared Error (MSE) and Peak-Signal to Noise Ratio. For the metrics, the binary reconstructed volumes were compared against a reference high quality image in each case.

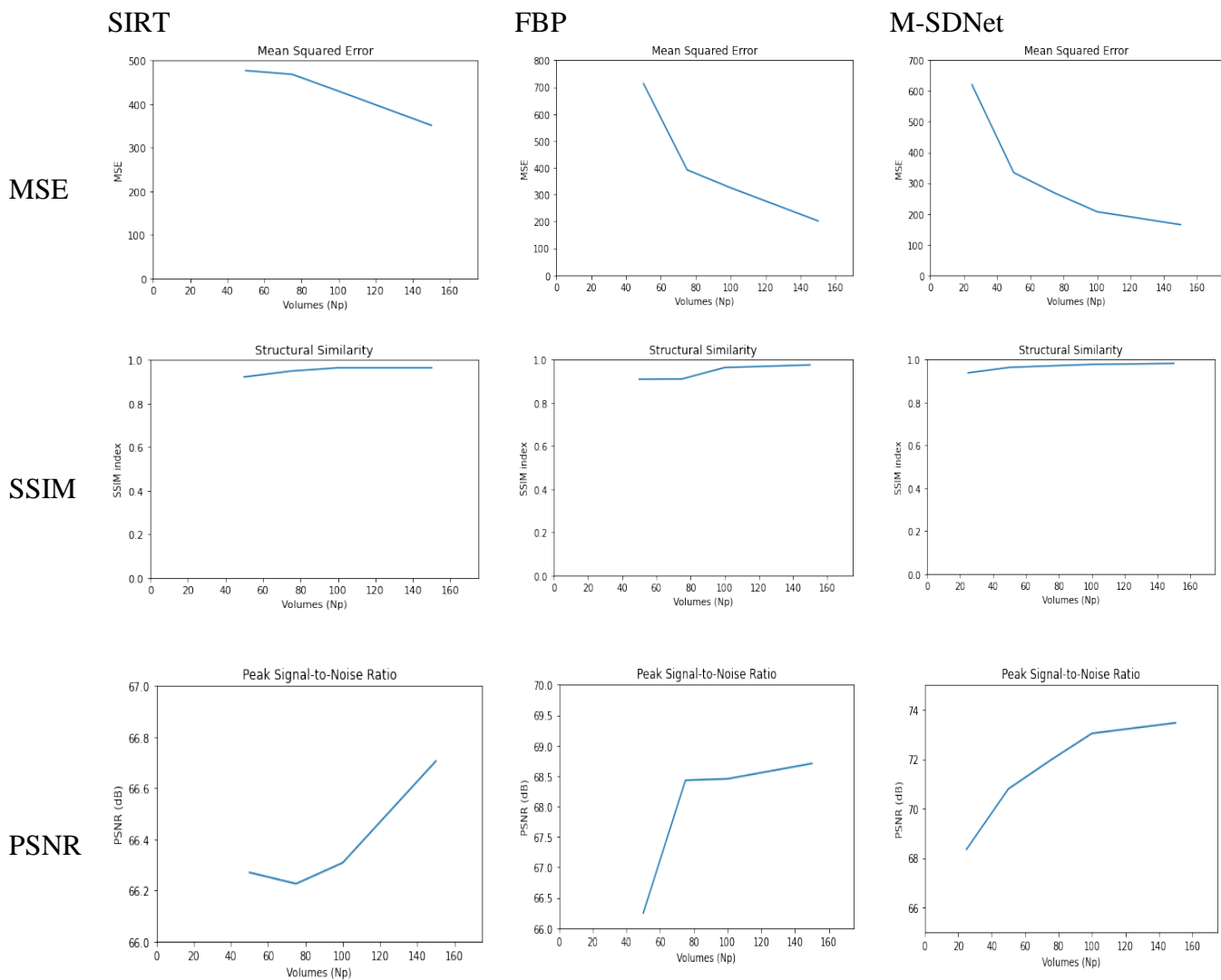


Figure 22: General metrics comparing FBP, SIRT and AI reconstructed volumes to the respective Reference: Mean Squared Error, Peak Signal-to-Noise Ratio and Structural Similarity index

The metrics shown in Figure 22 generally improve as the number of projections (Np) used in the reconstruction increase. For the Mean Squared Error (MSE), the FBP and M-SDNet algorithms

show the best reduction in error between Ref and Volumes as Np increased. For SIRT, the MSE slightly reduced from about 500 to about 350 between 50 projections and 150 projections. The MSE at 50 projections for FBP and M-SDNet were approx. 700 and 350 respectively. The influence of the dense neural network training involved in M-SDNet resulted in about 50% error reduction for a very small number of projections. The error reduction is less as Np increased.

The Structural Similarity Index (SSIM) was fairly consistent in pattern across algorithms. Generally, the reconstructed volumes were structurally similar to the Reference even at low Np.

The Peak Signal-to-Noise ratio (PSNR) showed a similar trend that noise reduced across the volumes as the number of projections used for the reconstruction increased.

Number and Volume Fraction of Pores:

The Figure below illustrates the influence of number of projections in the quantitative analysis of the different M-SDNet reconstructed volumes. The segmentation of the different volumes was done with threshold value range of 105-110. This was done to obtain an average value of cavity parameters given that the segmentation was entirely subjective. For the cavity parameters analysed;

- The min value represents its minimum value across the threshold range
- The max value represents its maximum value across the threshold range
- The average value is the mean of the parameter across the threshold range

The number of pores (cavities) in the different volumes were compared to the Reference (which is the high-quality volume reconstructed with FBP using 500 projections). From Figure 23, the relative error in the volume fraction of pores reduced as the number of projections increased. With 25 projections, the relative error in volume fraction of pores was calculated to be over 8%, with 75 projections the relative error had reduced to less than 2%. Similarly, the number of pores observed with 75 projections up to 150 projections show about 10% relative error, down from 40% relative error observed with 25 projections.

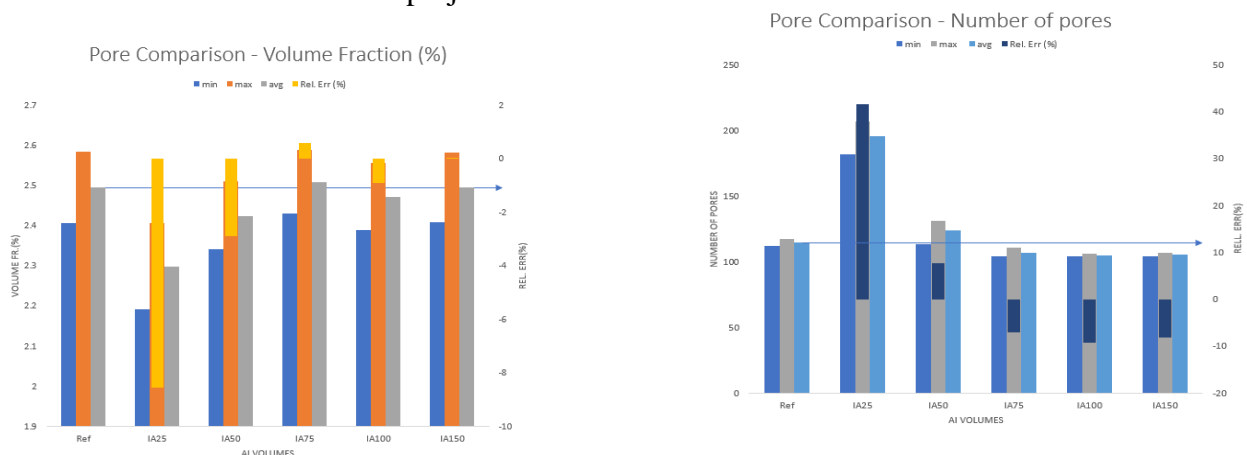


Figure 23: Pore comparison for AI volumes. Volume fraction (right), number of pores (left)

The wide error observed in 25 projections could be attributed to the splitting of pores and background artefacts incorporated into the segmented feature thereby increasing the number of pores and their volume fraction.



Segmented reference volume (left).
IA25 volume (right)

Figure 24:
Segmented

3D Pore Comparison:

Further quantitative comparison of the reconstructed volumes was carried out focusing on the cavities. Figure below shows a combined sphericity-volume plot showing all the AI reconstructed volumes with varying number of projections. The distribution of the pores shows that 1 cavity has a size of 5 orders of magnitude and hence less spherical than the rest. Also, more than 75% of all pores have volumes of 2 orders of magnitude. Very few cavities were almost fully spherical, and have very small volumes.

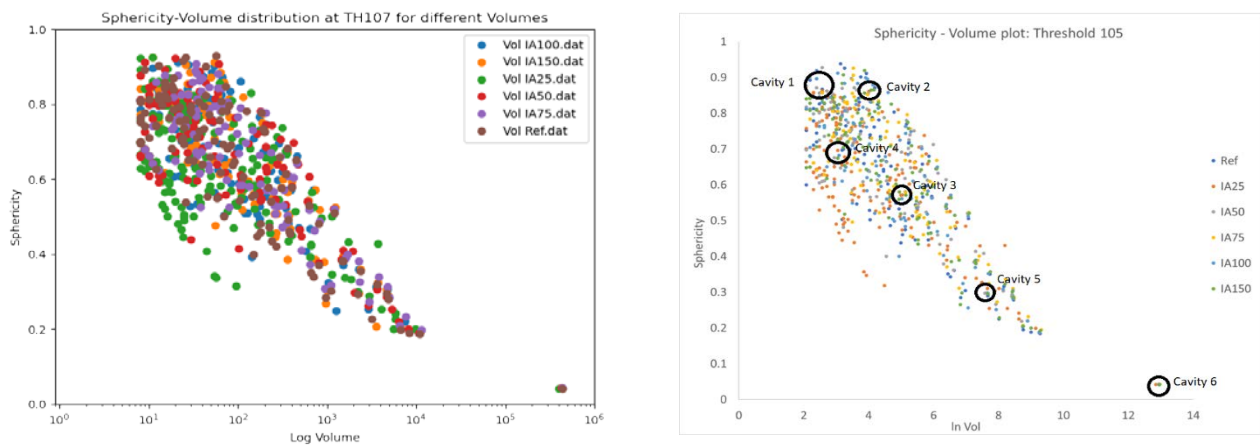


Figure 25: Sphericity – Volume plot of cavities in all AI volumes at threshold value of 105 (left). Sphericity – Volume plot of cavities showing selected cavities. (right)

A few representative pores were selected for comparison across the different AI volumes. The sphericity and volume of the pores were compared, and a 3D rendering of the pores was implemented using Mayavi toolbox in Python.

A 3D rendering of the cavities in the different IA volumes manually selected from the 6 circled zones in Figure 25 are shown in Figure 26 below;

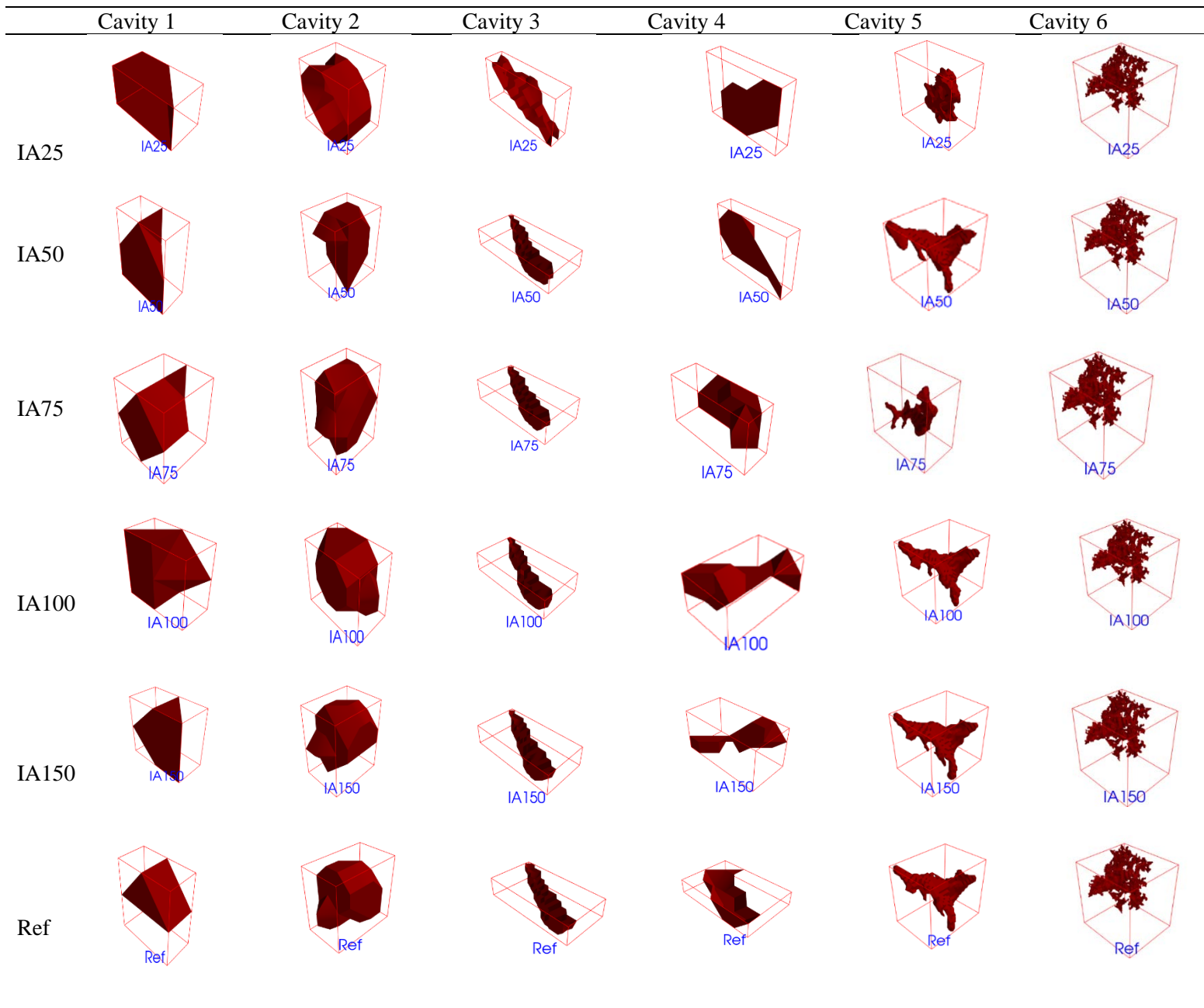


Figure 26: Manual tracking and comparison of 3D pores in various IA reconstructed volumes

In the manual tracking scheme, the figure above shows that larger cavities were easier to track across the different IA volumes. The errors observed as missing pixels in cavities 1 to 4 across the IA volumes could be due to segmentation error which could shrink cavity volumes.

An automatic particle tracking scheme, described in the Materials and Methods chapter, was also implemented to track single cavities across the various reconstructed IA volumes with respect to the Reference. Cavities in the Reference volume were tracked in the different reconstructed volumes using a limiting distance comparing their centres of gravity. Sphericity-volume plots of

matching cavities were plotted using python and rendered with Mayavi. An error-volume plot of the cavities showing spatial errors in distance from the center of gravity of same cavity in Reference and in the reconstructed IA volumes, are shown in Figure 27.

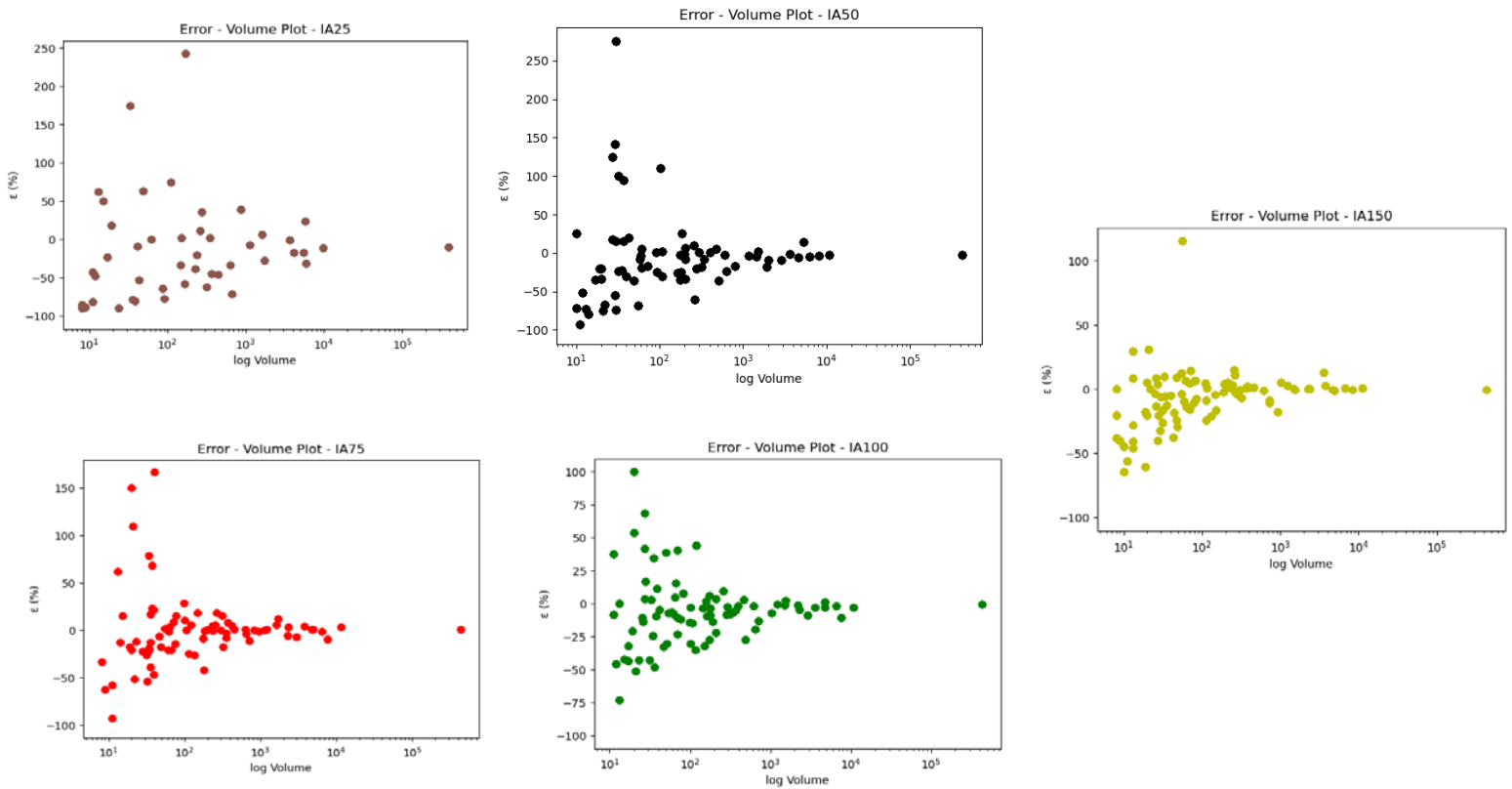


Figure 27: Error – Volume plot of cavities in different IA reconstructed volumes.

The plots in Figure 27 show that the relative error in the distance of cavities in the AI volumes compared to similar cavities in the Reference volume decreases generally as cavity volume increased. The biggest cavity, with volume over 100,000 cubic units showed near zero relative error across all the AI volumes, while smaller cavities had progressively smaller errors as number of projections used in the reconstruction increased. Cavities with volumes below 100 cubic units showed the widest disparity in error, varying between over $\pm 150\%$ relative error.

Generally, as has been inferred in previous analysis, using more projections to reconstruct a 3D volume yielded more accurate representation of the original sample.

The figures below show a sphericity – volume plot and 3D compilation of similar cavities from the different AI volumes with **small error** relative to the cavity in the Reference.

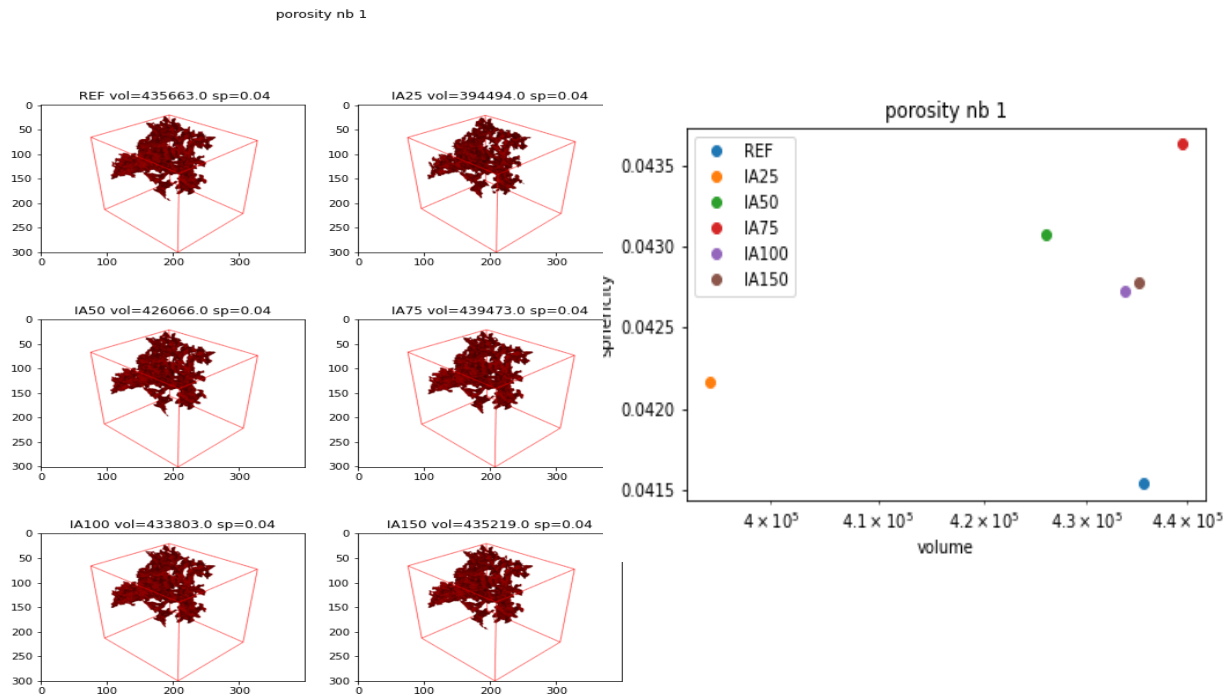


Figure 28: Cavity nb.1, with small relative error across AI volumes. 3D rendering (left), sphericity-volume plot (right).

The sphericity-volume plot in Figure 28 shows that the sphericity of the cavity nb.1 in the different AI volumes varied from 0.0415 – 0.435. The sphericity of the cavity in IA25 was closest to the REF, while its volume had the biggest deviation, about 15%, from that of the REF, compared to about 0.2% deviation in IA100 and IA150. With higher number of projections, as seen in IA100 and IA150, the volume of the cavities was closer to that in the REF. The sphericity of the cavities in IA100 and IA150 showed less than 3% deviation from that of the REF. The conclusion from this group of cavities is that larger cavities showed the least deviation in properties across the different IA volumes.

The figures below show a sphericity – volume plot and 3D compilation of similar cavities from the different AI volumes with **medium error** relative to the cavity in the Reference.

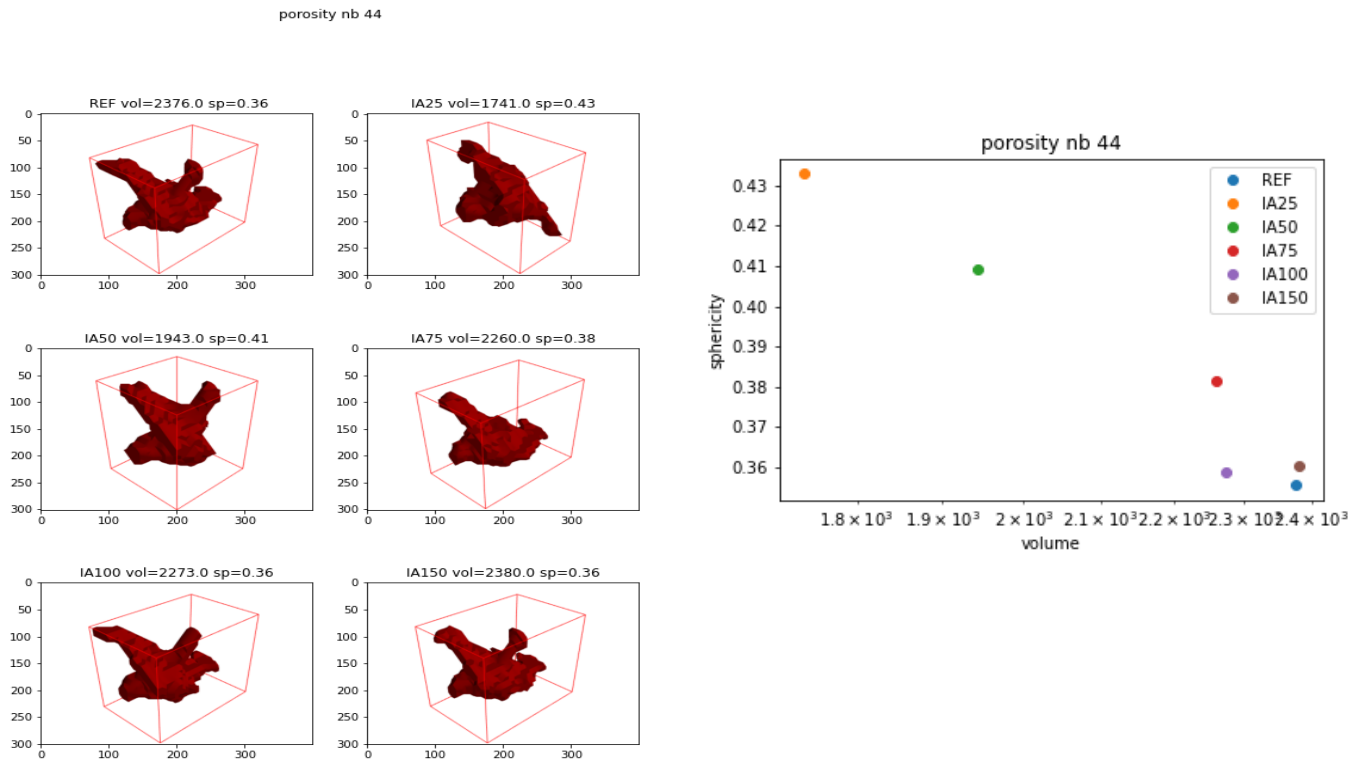


Figure 29: Cavity nb.44, with medium relative error across AI volumes. 3D rendering (left), sphericity-volume plot (right).

Figure 29 shows similarity in the cavities sampled in this region. The errors in the properties of the cavities relative to the Ref were not as minimal as found in Figure 28. The errors in the volumes of the cavities were in the range of $\pm 25\%$ and also are attributed to segmentation.

The figures below show a sphericity – volume plot and 3D compilation of similar cavities from the different AI volumes with high error relative to the cavity in the Reference.

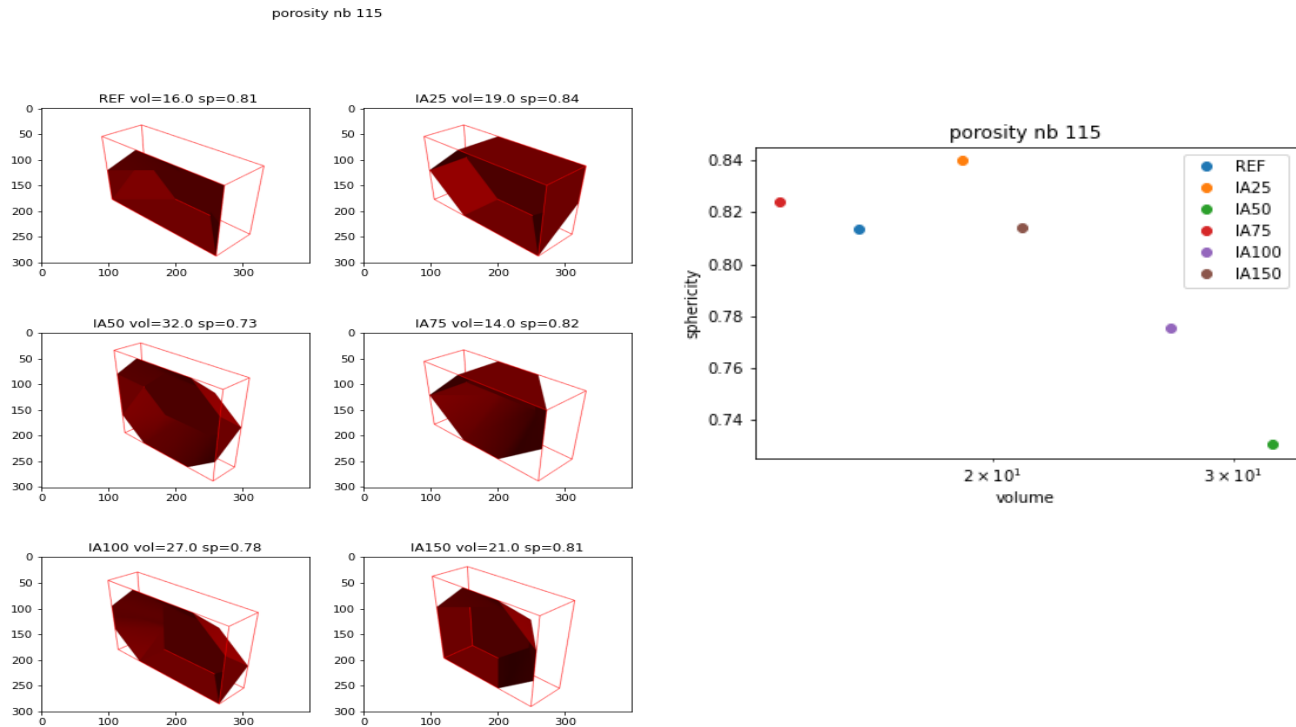


Figure 30: Cavity nb.44, with high relative error across AI volumes. 3D rendering (right), sphericity-volume plot (right).

Figure 30 shows a selection of cavities with volumes less than 100 cubic units. Given that the cavities are composed of few pixels, the wide value of relative errors is expected because a missing pixel in the reconstruction of the cavity would be more significant than a missing pixel in a very large cavity.

Influence of Number of Projections with Training on Binary Images (Al-Cu-Si sample)

In order to improve reconstruction of cavities in the IA volumes, the M-SDNet segmentation algorithm was used to generate binary images from FBP reconstructed volumes for the Al-Cu-Si sample scanned at the ESRF. This is the second strategy of the M-SDNet application described in the Materials and Methods chapter.

The target image was a high quality, 500 projections, FBP reconstructed volume while the input images were grey-level images obtained using FBP by varying the number of projections – 50, 75, 100, 150, 200 and 250. The target image was segmented with a threshold value of 95.

The input images and were trained simultaneously on the same PC with properties as: Linux Mint 17.3 and NVIDIA GK104GL Quadro K4200CUDA GPU over a period of 24 hours. The network tries to match features found in the input image with similar features in the segmented target image to produce a binary network output, by minimizing the error pixel by pixel according to an inbuilt loss function. For each iteration, the algorithm records current and best errors and proceeds with minimizing the error till it cannot reduce it further. There is no stopping criterion in the code, and hence after 24hours, it was observed that the best error had stayed constant over a time period. Plots of current error and best error as a function of the number of iterations are presented for each reconstructed volume. After the training, the model for each volume is saved as a .h5 file, and applied to the each of the grey-level images to produce an output which is cavity probability distribution: a grey-level representation of the cavities on black background.

The figure below shows a plot of the current and best errors as a function of the number of training epochs (number of iterations), obtained from the segmentation training of the reconstructed FBP50 on the right, and a representation of the ML training for FBP50 image on the left.

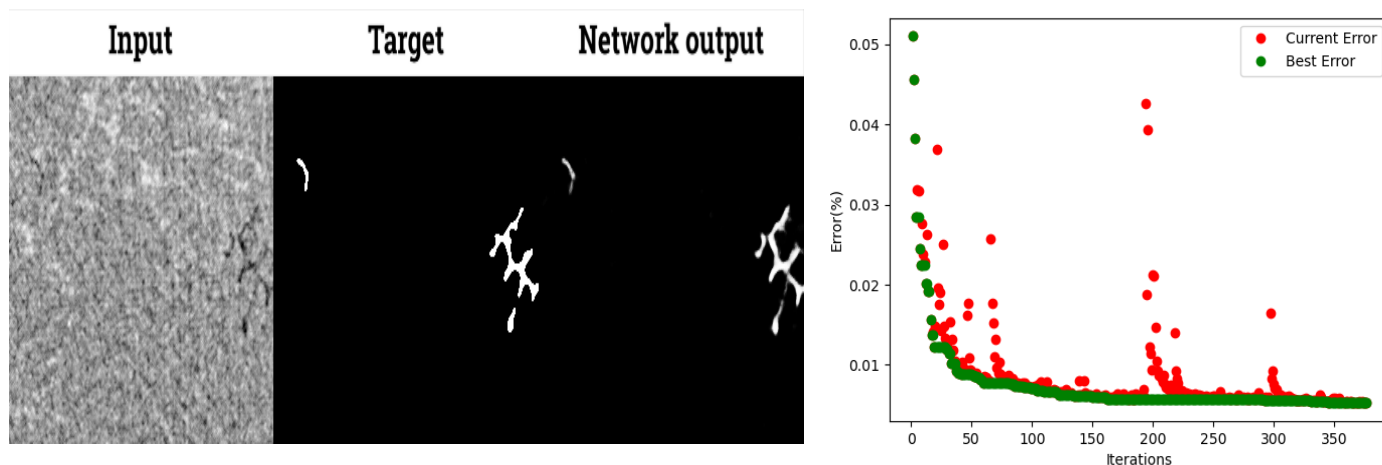


Figure 31: Single channel segmentation training for 50 projections(left). Training error vs iterations (right).

The figure below shows a plot of the current and best errors as a function of the number of training epochs (number of iterations), obtained from the segmentation training of the reconstructed FBP volumes.

From the figure of errors shown above, the segmentation algorithm sharply decreased the best error obtainable between target and input images in the first 50 iterations, for almost all the input and target, largely due to the noise in the input image. It can be thus deduced from the plot that the minimum number of iterations to obtain a quality network output is 100 iterations, translating to about 10 hours of training. This estimate does not take into account the GPU capacity given that all six training cases were run simultaneously thereby affecting processing time for each.

The network output of the segmentation training on the FBP images are shown in Figure and compared with the manual segmentation of similar volumes.









	Manual Segmentation	M-SDNet Output
FBP50		
FBP75		
FBP100		
FBP150		

Figure 32: Qualitative comparison of M-SDNet segmentation output and manual segmentation of FBP reconstructed volumes.

A qualitative comparison of the 2D images in Figure 32 shows that the M-SDNet output had better reconstruction of the cavities than the manually segmented FBP images. With M-SDNet and at least 50 projections, reconstruction of images could be achieved with higher accuracy than with FBP.

Analysis of Network Output Volumes:

The network output volumes were segmented and quantitatively analysed considering the number of cavities, volume fraction of cavities, and particle tracking and mismatch scheme with reference to the target image.

Given that the network output volumes contained cavities in grey-level but on black background, there was the need to segmentate the images in order to analyse the particles.

To obtain an optimal threshold value for the segmentation, segmentation was carried out across a range of values and the resulting binary images were compared to the Reference binary image used for the training. The SSIM index was used for the comparison. The result of this procedure is shown in Figure 35 below;

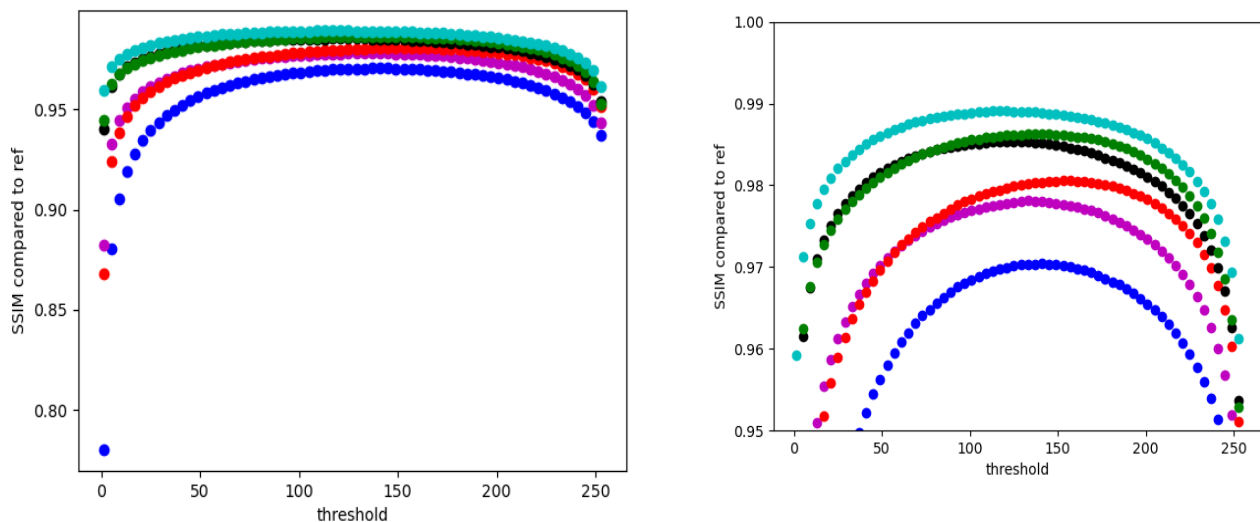


Figure 33: SSIM values for different output volumes compared to Ref, as a function of threshold value. Cropped section of plot (Right)

The plot above shows that the optimal threshold value needed to obtain images very similar to the Reference varied from volume to volume, but could be found in the range of 120 to 170.

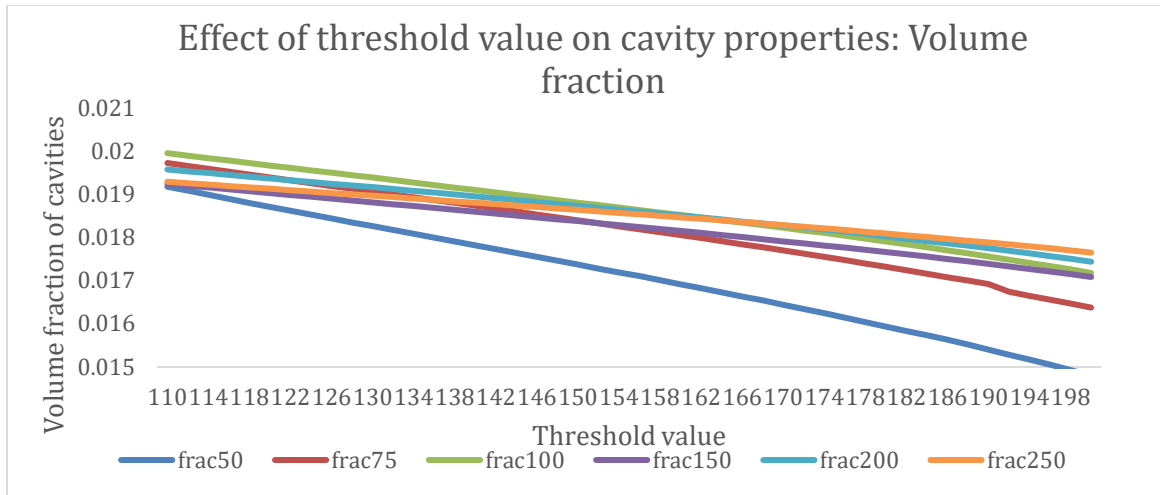


Figure 34: Effect of threshold values on number of pores across segmented output volumes

It is observed that the volume fraction of cavities in the different output volumes decreased as threshold value used for segmentation increased. 50 projections showed the most decrease as threshold value increased. The volume fraction for 100, 150, 200 and 250 projections had similar variation as threshold value increased.

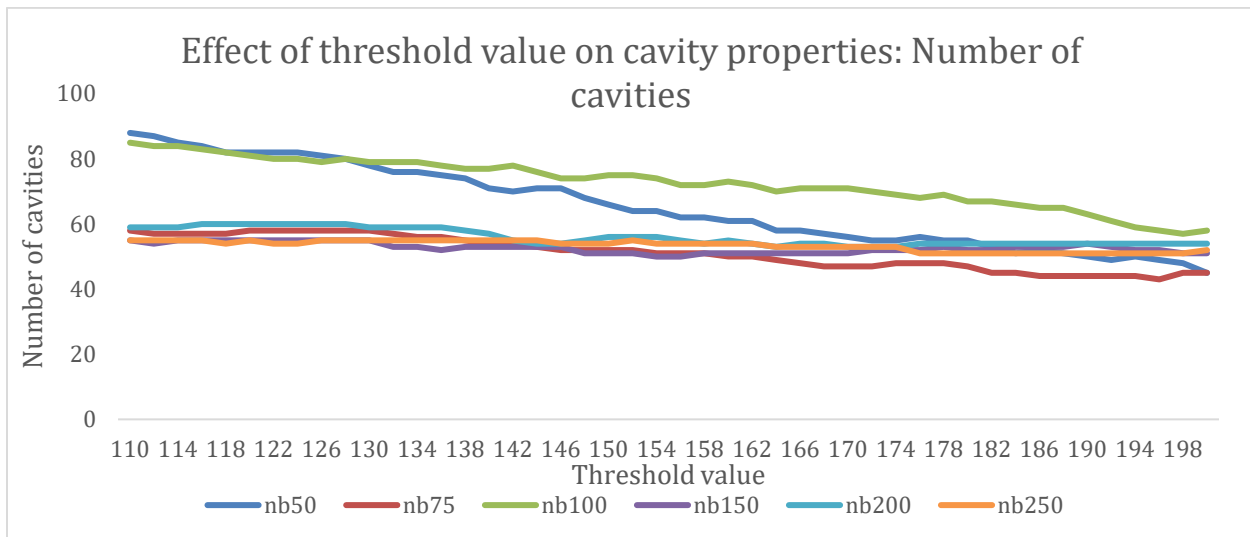


Figure 35: Effect of threshold value on number of cavities for network output volumes as function of threshold value.

The result in Figure 35 shows that the number of cavities in the output volumes maintained very similar values even as the thresholding value increased, as expected. However, 100 projections and 50 projections showed very wide deviation from the rest and only converged as the thresholding value approached 200.

The reason for this is not well understood given that the training time for all the images were the same. More study would need to be carried out to properly understand the segmentation algorithm of the M-SDNet architecture.

The automatic particle tracking scheme applied to the IA volumes and the output volumes from the segmentation training resulted in cavity matching and comparison already presented for the IA

volumes in Figure 28 to 30. The number of mismatched cavities were also analysed to compare the two training strategies and the results are shown in Figure 36.

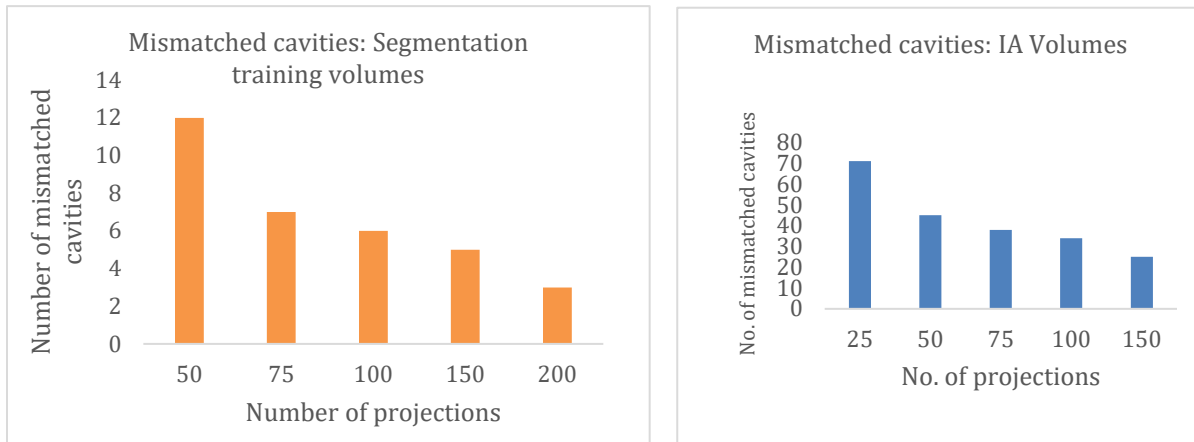


Figure 36: Number of mismatched cavities as function of projections for IA volumes and segmentation training output volumes.

The segmentation training resulted in far fewer mismatched cavities than the grey-level training. It can be seen that with a focus on cavities, the segmentation training better reconstructed the cavities with respect to the Reference image. A focus of training for the intermetallics would use the grey-level training but with a greater number of projections as already seen from Figure 19.

In order to test the possibility of building a database of network parameters (.h5 – network parameters) for samples with similar microstructures. The network parameter in machine learning is a value which controls the learning process. To enable this, the two volumes must have the same grey scale and dimensions.

Network parameters from Al-Cu-Si Sample 1 training were applied to slices of Sample 2. The results for 50 projections and 100 projections are shown in the figures below. The results show that this could be a possibility and should be researched further.

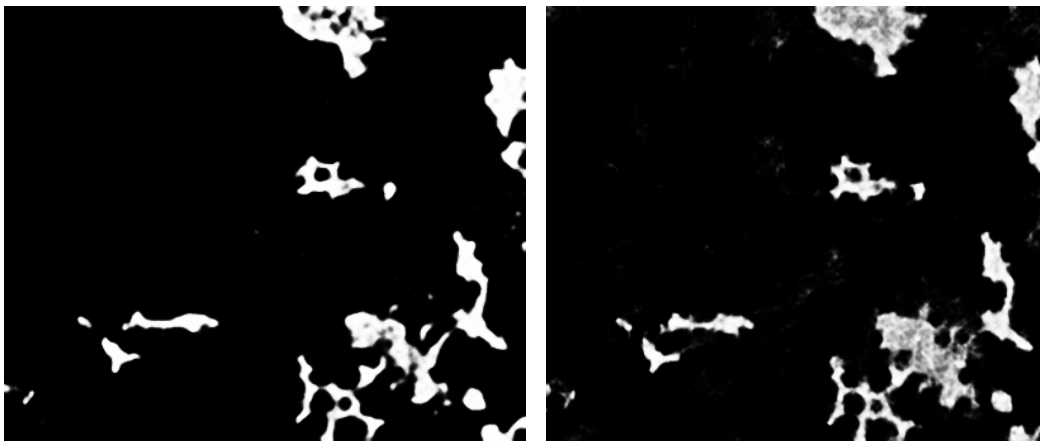


Figure 37: Results of Al-Cu-Si Sample1 100 projections training:100proj volume trained with target (left). 100proj volume trained with Sample2 100proj .h5 file (right).

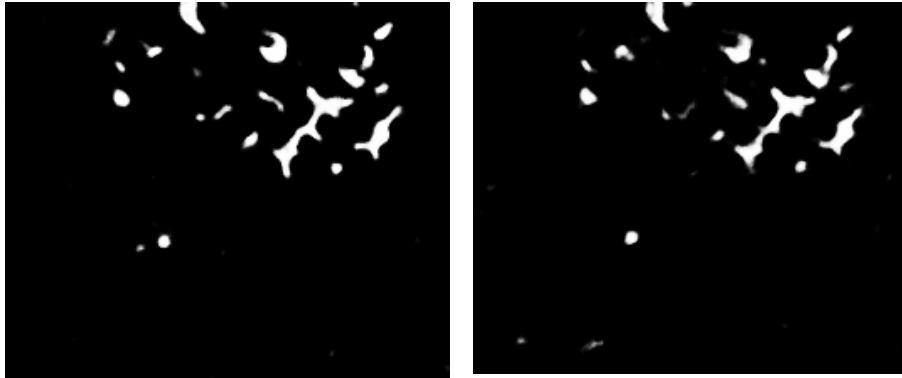


Figure 38: Results of Al-Cu-Si Sample1 50 projections training: (Left) 100proj volume trained with target, (Right) 100proj volume trained with Sample2 50proj .h5 file

Training on 316L(N) Data

The 316L(N) sample scanned at the ESRF was reconstructed with a python implemented FBP algorithm using Astra toolbox with standard toolbox parameters as shown in Figure 13 of the Materials and Methods chapter.

The M-SDNet segmentation algorithm was applied on the low-quality grey-level input images (125projections and 250 projections) with the segmented high-quality image (1250 projections) as the target.

The result of the network training is shown in the figures below.

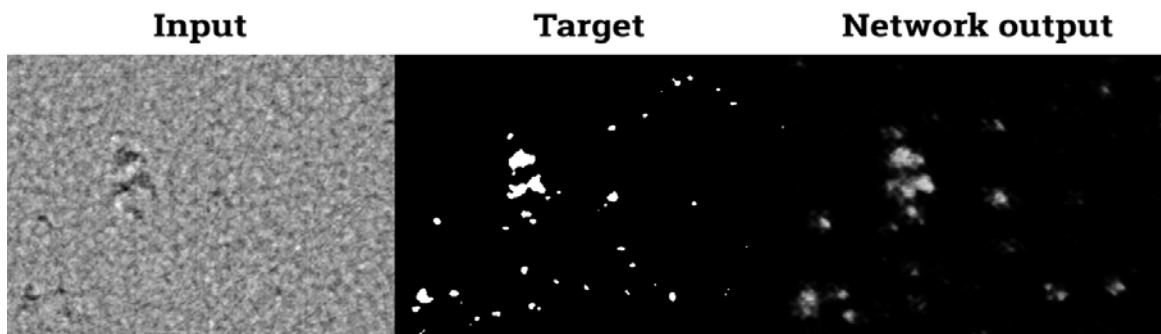


Figure 39: M-SDNet Segmentation training on 125proj reconstructed volume of 316

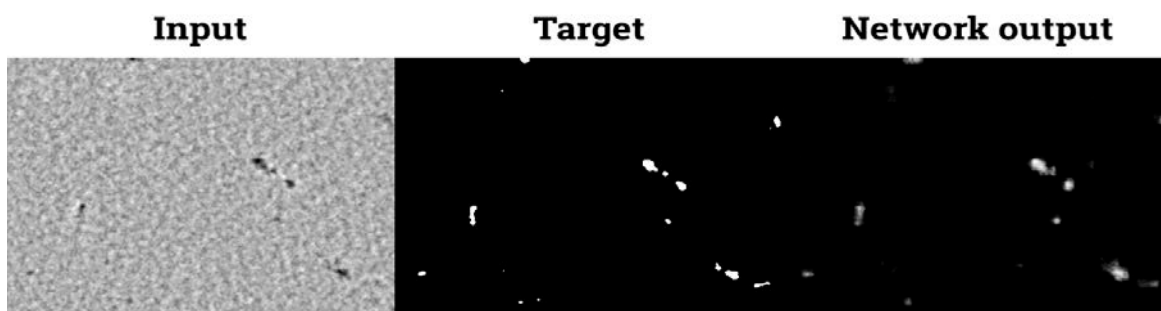


Figure 40: M-SDNet Segmentation training on 250proj reconstructed volume of 316

A visual inspection of the network output in the two figures above show that with 125 projections, the training is severely limited in reconstructing the features. Over 50% of the small cavities were not captured in the network output. For 250 projections, the network output is better than with 125 projections, with fewer small cavities missing. With 416 projections and 650 projections, the results are expected to fully reconstruct the features of the high-quality image. This would represent a gain of a factor of 3 and 2 respectively. Optimally leading to a reduction in scan time, dose and storage space for acquired data.

Effect of Resolution: Improving Lab Experimental Data

The influence of M-SDNet algorithm on improving low quality images obtained from in-situ tomography was studied. Images of Al-Cu-Si sample reconstructed with 96 projections for $1\mu\text{m}$ resolution, average frame of 5 frames, and a scan rate of 1 frame/second, were trained with the M-SDNet regression algorithm. A small region of interest – $759 \times 574 \times 250$, was selected to reduce training time and computer storage space. High quality images reconstructed with 1440 projections at $1\mu\text{m}$ resolution were used as ‘target’ in the training and validation sets, while the low-quality slices from the in-situ data were used as ‘input’ in the training and validation sets.

The result of the regression training for the low-quality image after a 24hr training is shown in the figure below.

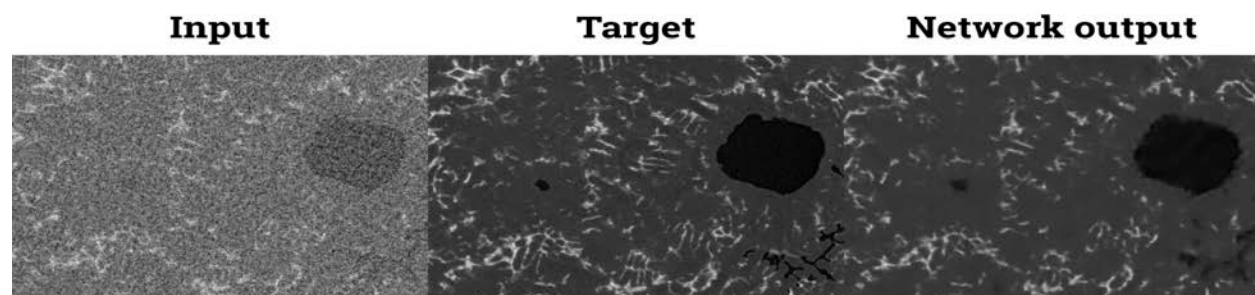


Figure 41: Regression training on Al-Cu-Si sample FBP reconstruction using 96 projections

It can be seen from Figure that background noise in the input image was reduced significantly, and most features were retrieved. The network output has PSNR value of 75% compared to 65% of the input image. A cropped section of the pores is shown in Figure 42.

For the high-quality target image, the scan time was around 7200 seconds. The low-quality image was scanned in about 480 seconds. The gain in time by using 96 projections for the reconstruction is 6720 seconds. An improvement in the quality of the 96 projections image would reduce scan time by a factor of 15. With 480 projections, the image quality is expected to be much higher and thus a significant reduction in scan time.

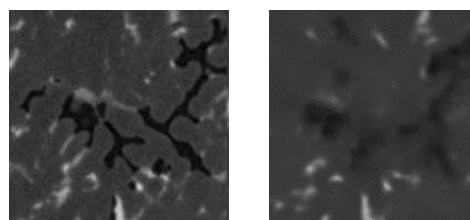


Figure 42: Cropped section of some pores in Fig. 41

Improving In-Situ Experimental Data

For in-situ laboratory experiments, a furnace, heat treatment or compacting device would have to be placed between source and detector, as shown in Figure 2 of this report, thereby affecting the maximum possible resolution of x-ray tomography to be done. The experiments carried out in the SIMAP laboratory show that for available furnaces, a minimum distance of 20mm has to be maintained between source and sample. This arrangement limits the obtainable resolution to about $4.3\mu\text{m}$. During in-situ experiments, there is need for fast acquisition hence frame rate is reduced to about 1fps or less, and total number of projections is limited. To improve the resolution, smaller furnaces and in-situ devices have to be developed to minimize SOD. M-SDNet algorithm was applied to denoise experimental data acquired from 288 projections, 1 fps, and 1 average frame, at an SOD of 12.9mm.

A second small region of interest was cropped corresponding to FOV of $620 \times 464 \times 400$. The result of the regression training is shown in the figure below

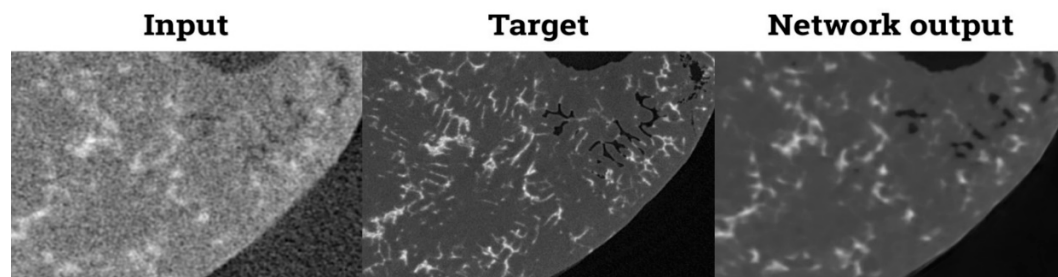


Figure 43: M-SDNet regression training on in-situ 288proj reconstructed volume of Al-Cu-Si sample

Experimental data showed more noise even in the network output volume with many features not adequately recovered. This could be attributed to x-ray source and detector properties. The use of a direct counting detector (Pixirad) would yield higher quality projections due to more photons directed counted.

In order to simulate the use of a direct counting detector, which would produce less noisy images, the high-resolution acquisition with 1440 projections was scaled up and down by a factor of 4, to degrade the images. This degraded image was then fed into the algorithm for regression training as low-quality input image while the high-resolution image was retained as the 'target'.

The result of the training is shown in Figure 44 below.

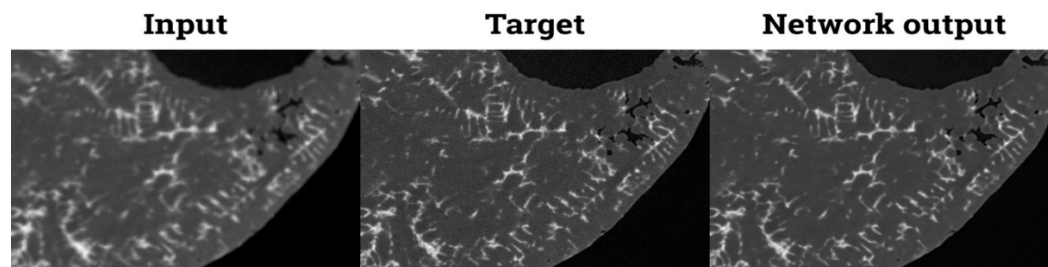


Figure 44: Regression training on degraded high-quality image

The degraded input volume, representative of lab acquisition with less noise, The network output correlates with the results of the 'denoising' operation presented by Hendrikson et al in [13], as well as by Pelt et al presented in [4], indicating that the M-SDNet algorithm could be a powerful tool for image processing and can significantly reduce acquisition time for x-ray imaging.

CHAPTER V: CONCLUSION AND PERSPECTIVES

In this thesis, we have studied the application of Mixed-Scale Dense neural network architecture (M-SDNet) in the improvement of images from synchrotron and laboratory x-ray sources. The main objective was to quantitatively determine the effectiveness of this algorithm for the improvement of in-situ laboratory tomography reconstructions given the challenges presented by such experiments and the need to still obtain high resolution images with limited data, and in the shortest possible scan time. The proposed algorithm has shown to be efficient compared with existing tomographic reconstruction algorithms.

A highlight of specific conclusions from the study include:

1. When presented with grey-level input volumes reconstructed with limited number of projections and a grey-level high quality 'Target' volume reconstructed with 500 projections, the M-SDNet training output were of very high quality compared to images reconstructed with FBP and SIRT algorithms. Based on SSIM and MSE values, the network output using at least 75 projections were of similar quality with the Reference - 500 projections reconstructions using FBP. This is of importance to in-situ tomography because of the demonstrated reduction in number of projections and thus scan time.
2. Quantitative analysis focusing on cavities found in the Al-Cu-Si sample studied showed that with 75 projections, 100 projections and 150projections, cavity properties such as sphericity and volume were also adequately reconstructed with minimal errors.
3. A second strategy in the M-SDNet architecture is to train the grey-level low quality images with a segmented high-quality image as 'Target'. This approach focusing on the accurate reconstruction of cavities was applied to low quality FBP reconstructed volumes of our sample. The result of this segmentation training were volumes with grey-level cavities in a black background, with accompanying probability density. These output volumes were segmented for cavities and quantitatively analysed focusing on specific parameters of the cavities.
4. A particle tracking scheme was applied to results from the two M-SDNet approaches highlighted before. This scheme matches cavities found in the Reference image with those in the output images of the network based on their centres of gravity. It was observed that the second strategy of training with a binary target volume yielded more matching cavities that the first strategy of training with a grey-level target.
5. With the M-SDNet algorithm, the required number of projections needed to reproduce high quality images is thus reduced by a factor of 3 at least, when comparing the 150 projections with the Reference 500 projections FBP reconstruction.
6. Based on results obtained from training with two Al-Cu-Si samples with slightly different compositions, a database is proposed to compile .h5 (network parameter) files for samples with similar microstructures which could be used interchangeably. This would reduce computing time.

While this study has highlighted some of the benefits of using the M-SDNet algorithm for in-situ tomography, it is not exhaustive and therefore further study could be carried out on some key areas. Given that the output of the binary training is a grey-level probability distribution of

cavities, and that the segmentation requirement after the training is carried out for both strategies, more research could be done to obtain a more objective way of carrying out segmentation for network output images.

The acquisitions made in the laboratory representative of in-situ conditions were done with a flat-panel detector, with a lot of noise in the images. Training with the M-SDNet algorithm did not give very high-quality reconstruction of some cavities as expected. However, a degraded image obtained from scaling a high-resolution image up and down, yielded expected results from the training. Further study could be done with a direct counting detector to eliminate some background noise in the images while doing in-situ experiments.

The proposed database of .h5 files for samples with similar microstructural properties is also another area of interest for further study. With that, less computing time would be needed for analysing

Appendix:

Automatic Cavity Tracking Code implemented in Python.

```
import matplotlib.pyplot as plt

import numpy as np

import math

def lecture_dat(name,col,xg,yg,zg,vol,volm,surf,sp):

    fichier = open(name, "r")

    data = fichier.readlines()

    nb=len(data)-1

    # load data of file .dat with volume above 8 pixel

    for i in range(0,nb):

        line=data[i+1]

        splitline=line.split(' ')

        col.append(float(splitline[0]))

        xg.append(float(splitline[1]))

        yg.append(float(splitline[2]))

        zg.append(float(splitline[3]))

        vol.append(float(splitline[4]))

        volm.append(float(splitline[5]))

        surf.append(float(splitline[6]))

        sp.append(float(splitline[8]))
```

```

return(nb,col,xg,yg,zg,vol,volm,surf,sp)

coll=[]

xg1=[]

yg1=[]

zg1=[]

voll=[]

volm1=[]

surf1=[]

sp1=[]

plt.close('all')

# name of the file

liste=[25,50,75,100,150]

# limit on the distance between center of gravity between ref and IA

dlim=5

#opening ref dat file

fileref='refbin107lab8'

print("reffile is :"+fileref)

lecture_dat(fileref+".dat",coll,xg1,yg1,zg1,voll,volm1,surf1,sp1)

#creating necessary tables

# tab_indices store the indices of pores and put zeros when pore is not found in IA

tab_indice=np.zeros((len(coll),6)) #indices ref cavities

# tab_vol store the volume of pores and put zeros when pore is not found in IA

tab_vol=np.zeros((len(coll),6)) #indices IA cavities 0 is put if not find

```



```
tab_sp=np.zeros((len(col1),6)) #indices IA cavities 0 is put if not find
```

```
tab_dv=np.zeros((len(col1),6)) #indices IA cavities 0 is put if not find
```

```
for i in range(0,len(col1)):
```

```
    tab_indice[i][0]=col1[i]
```

```
    tab_vol[i][0]=vol1[i]
```

```
    tab_sp[i][0]=sp1[i]
```

```
    cpt=1
```

```
for name in liste:
```

```
    dmin=1e10
```

```
    dvmin=1000
```

```
    file='IA%dbin107lab8' %name
```

```
    #print(file)
```

```
    col2=[]
```

```
    xg2=[]
```

```
    yg2=[]
```

```
    zg2=[]
```

```
    vol2=[]
```

```
    volm2=[]
```

```
    surf2=[]
```

```
    sp2=[]
```

```
    lecture_dat(file+".dat",col2,xg2,yg2,zg2,vol2,volm2,surf2,sp2)
```

```

for j in range(0,len(col2)):

    d=math.sqrt((xg1[i]-xg2[j])**2+(yg1[i]-yg2[j])**2+(zg1[i]-zg2[j])**2)

    dv=abs(vol2[j]-vol1[i])/vol1[i]

    if (d<dlim and d<dmin and dv<dvmin):

        tab_indice[i][cpt]=col2[j]

        tab_vol[i][cpt]=vol2[j]

        tab_sp[i][cpt]=sp2[j]

        ind=j

        dmin=d

        dvmin=dv

    cpt=cpt+1

np.savetxt("tab_indices.csv", tab_indice, delimiter=";")

np.savetxt("tab_vol.csv", tab_vol, delimiter=";")

np.savetxt("tab_sp.csv", tab_sp, delimiter=";")

np.savetxt("tab_dv.csv", tab_dv, delimiter=";")

plt.figure(1)

for i in range(0,6):

    tab_dv[:,i]=((tab_vol[:,i]-tab_vol[:,0])/tab_vol[:,0])*100

    plt.semilogx(tab_vol[:,i],tab_dv[:,i],'o')

plt.show()

np.savetxt("tab_dv.csv", tab_dv, delimiter=";")

np.savetxt("tab_vol.csv", tab_vol, delimiter=";")

```

References

- [1] Z. Yan, C. L. Martin, D. Bouvard, D. Jauffrès, P. Lhuissier, L. Salvo and L. Olmos, “Coupling in-situ X-ray micro- and nano-tomography and discrete element method for investigating high temperature sintering of metal and ceramic,” in *Powders & Grains*, 2017.
- [2] G. Mobus and B. J. Inkson, “Nanoscale tomography in materials science,” *Materials Today*, 2007.
- [3] J. e. a. Villanova, “Fast in situ 3D Nanoimaging: a New Tool for Dynamic Characterization in Materials Science,” *Materials Today*, 2017.
- [4] D. M. Pelt, K. J. Batenburg and J. A. Sethian, “Improving Tomographic Reconstruction from Limited Data Using Mixed-Scale Dense Convolutional Neural Networks,” *Journal of Imaging*, 2018.
- [5] D. M. Pelt and J. A. Sethian, “A Mixed-scale Dense Convolutional Neural Network for Image Analysis,” *PNANS*, 2018.
- [6] E. F. Oliveira, S. B. Melo, C. C. Danta, D. A. A. Vasconcelos and a. L. F. Cadiz, “Comparison Among Tomographic Reconstruction Algorithms with a Limited Data,” in *International Nuclear Atlantic Conference - INAC 2011*, Belo Horizonte, MG, Brazil, 2011.
- [7] S. Coban and et.al, “Assessing the Efficacy of Tomographic Reconstruction Methods through Physical Quantification Techniques,” *Meas. Sci. Technol*, 2021.
- [8] G. Wang, H. Yu and B. D. Man, “An outlook on x-ray CT research and development,” *International Journal of Medical Physics Research and Practice*, 2008.
- [9] A. Kak and M. Slaney, “Principles of Computerized Tomographic Imaging,” in *Society of Industrial and Applied Mathematics*, Philadelphia, USA, 2001.
- [10] J. Wang, J. Liang, J. Cheng, Y. Guo and L. Zeng, “Deep learning based image reconstruction algorithm for limited-angle translational computed tomography,” *PLOS ONE*, 2020.
- [11] L. Y, B. Y and H. G, “Deep learning,” *Nature*, vol. vol. 521, no. no. 7553, p. pp. 436–444, 2015.
- [12] D. M. Pelt and B. K. J, “Fast Tomographic Reconstruction From Limited Data Using Artificial Neural Networks,” *IEEE Transactions on Image Processing*, vol. vol. 22, no. no. 12, p. pp. 5238, 2013.
- [13] A. A. Hendriksen¹, M. Bührer, L. Leone, M. Merlini, N. Vigano, D. M. Pelt, F. Marone, M. d. Michiel and & K. J. Batenburg, “Deep Denoising for Multi-dimensional Synchrotron X-ray Tomography Without High-quality Reference Data,” *Scientific Reports | Nature*, vol. 11:11895, 2021.
- [14] M. H. Kabir, “Convolutional Neural Network,” ResearchGate, Bangladesh, 2021.

- [15] M. Basavarajaiah, 6 Basic Things to Know About Convolution, <https://medium.com/@bdhuma/6-basic-things-to-know-about-convolution-daef5e1bc411>, 2019.
- [16] R. Schoonhoven, J.-W. Buurlage, D. M. Pelt and a. K. J. Batenburg, "Real-time Segmentation for Tomographic Imaging," in *IEEE 30th International Workshop on Machine Learning for Signal Processing (MLSP)*, 2020.
- [17] D. Asamoah, E. O. Oppong and J. Danso, "Measuring the Performance of Image Contrast Enhancement Technique," *International Journal of Computer Applications*, vol. 181, no. No. 22, 2018.
- [18] Z. Wang, A. C. Bovik, H. R. Sheikh and E. P. Simoncelli, "Image Quality Assessment: From Error Measurement to Structural Similarity," *IEEE TRANSACTIONS ON IMAGE PROCESSING*, vol. 13, 2004.
- [19] B. Muehlhauser, "Optimizing Image Signal to Noise Ratio Using Frame Averaging," North Star Imaging Blog, 2015.
- [20] W. V. AARLE, W. J. PALENSTIJN, J. CANT, E. JANSSENS, F. BLEICHRODT, A. DABRAVOLSKI, J. D. BEENHOUWER, K. J. BATENBURG and A. J. SIJBERS, "Fast and flexible X-ray tomography using the ASTRA Toolbox," in *Optical Society of America*, 2016.
- [21] M. D. Abramoff, M. P. J and S. J. Ram, "Image Processing with ImageJ," *Biophotonics International* , vol. 11, no. 7, pp. 36 - 42, 2004.
- [22] V. Boulos, L. Salvo, P. Lhuissier, V. Fristot and D. Houzet, "Investigating Performance Variations of an Optimized GPU-porting Granulometry Algorithm," in *18th International European Conference on Distributed Computing* , Rhodes Island, Greece, 2012.
- [23] P. Ramachandran and G. Varoquaux, "Mayavi: 3D Visualization of Scientific Data," *IEEE Computing in Science and Engineering*, vol. 13, no. 2, pp. 40-51, 2011.
- [24] S. V. d. Walt and et.al, "Scikit-image: Image Processing in Python," *PeerJ*, vol. 2, no. 453, 2014.
- [25] A. A. Hendriksen, D. M. Pelt, W. J. Palenstijn and S. B. C. a. K. J. Batenburg, "On-the-Fly Machine Learning for Improving Image Resolution in Tomography," *Applied Sciences*, 2019.
- [26] V. Boulos, L. Salvo, V. Fristot, P. Lhuissier and D. Houzet, "Investigating Performance Variations of an Optimized GPU-porting Granulometry Algorithm," in *18th International European Conference on Parallel and Distributed Computing*., Rhodes Island, Greece, 2012.